

DESIGN REPORT
(T1706293) VER.4

KAGRA photon calibrator

Author:

Y. INOUE, S. Haino, N. Kanda, T. Tomaru, T. Yamamoto, and
T. Yokozawa
on the behalf of Calibration sub-group

KAGRA
Calibration subsystem

May 2, 2017



Abstract

KAGRA
Calibration subsystem

KAGRA photon calibrator

by Y. INOUE, S. Haino, N. Kanda, T. Tomaru, T. Yamamoto, and T. Yokozawa
on the behalf of Calibration sub-group

Accurate calibration of the output of the Gravitational Wave (GW) signal is crucial to determine the physics parameters of the sources. The primary tools used in the advanced GW detectors are photon calibrators based on the radiation pressure. In this document, we report the design of the KAGRA photon calibrator in order to achieve the absolute accuracy of several % to meet the calibration requirements of second-generation GW detectors in the new era of GW astronomy.

Acknowledgements

We cordially thank Prof. Rick Savage of LIGO Hanford Observatory who strongly encouraged and supported this work by sharing all the technical details and giving numerous critical comments and suggestions, together with LIGO calibration team, particularly, Dr. Evan Goetz, Dr. Kiwamu Izumi, Mr. Sudarshan Karki, Dr. Peter King, Dr. Jeff Kissel, Mr. Travis Sadecki, Mr. Darkhan Tuyenbayev and others. We are greatful for the technical supports of KEK and Academia Sinica particularly by Ayako Hagiwara, Chih-hsun Lin, Yoshikazu Namai, Shinichi Terashima, and Ayako Ueda. We thank Dr. Tomotada Akutsu who helped us to fix the in-vacuum design. KAGRA project is supported by MEXT and JSPS in Japan as well as its collaborating institutes. YI and SH acknowledge the supports by Academia Sinica and MoST in Taiwan.

Contents

Abstract	iii
1 Introduction	1
1.1 Calibration of a Gravitational-Wave detector	1
1.2 Roles of the photon calibrator	2
1.3 Schedule of KAGRA	2
1.4 Calibration requirements from data analysis	3
2 Photon calibrator	5
2.1 Photon calibrator	5
2.2 Purpose of photon calibrator	6
2.2.1 Interferometer Calibration	6
2.2.2 Hardware injection test	8
2.2.3 Photon pressure actuator	9
2.3 Calibration line of KAGRA	9
3 Instruments descriptions	11
3.1 Layout of Photon calibrator	11
3.2 Placement of modules	11
3.3 Transmitter (Tx) module	13
3.3.1 Fiber laser	13
3.3.2 Beam shutter	17
3.3.3 Zeroth order half wave plate	17
3.3.4 Polarizer	17
3.3.5 Lens	18
3.3.6 Mirror	20
3.3.7 Optical mount with Pico-motor	20
3.3.8 Beam splitter	22
3.3.9 Optical follower servo	22
3.3.10 Photo detector	23
Cover	23
InGaAs detector	23
Electrical Circuit	25
3.3.11 Beam sampler	25
3.3.12 2 inch integrating sphere	27
3.3.13 Structure	27
3.4 Periscope	27
3.4.1 Geometric optics	27
3.4.2 View port window	29
3.4.3 Mirrors	31
3.5 Receiver module	31
3.5.1 6 inch Integrating sphere	32
3.5.2 Mirror	32

3.5.3	QPD	33
3.6	Camera module	33
3.6.1	Camera	33
3.6.2	Telescope	33
3.6.3	Focuser	33
3.6.4	View port window	33
3.6.5	Mirror	36
3.6.6	Illuminator	36
3.7	MEDM	36
3.8	Summary	36
4	Elastic deformation	39
4.1	Perfect Cylinder model	39
4.1.1	Modal displacement parameterization	39
4.1.2	Optimal beam position scan	41
4.2	Real ETM model	42
5	Absolute power calibration	47
5.1	Calibration in LHO	49
5.2	Calibration in end-station	49
5.3	Summary	51
6	Beam position monitor	53
6.1	Installation	53
6.2	Operation	53
6.3	Demonstration test	54
6.4	Summary	56
7	Future upgrades	59
7.1	Two AOM	59
7.2	KAGRA Gold Standard	59
8	Summary	63
A	Propagation of calibration errors into the estimated source parameters	65
A.1	DARM feedback loop modeling	65
A.2	Waveform modeling	68
	Bibliography	71

List of Figures

2.1 Frequency dependence of maximum displacement by KAGRA Pcal. Assumption 1: Using total laser power to one frequency. Assumption 2: pessimistic estimation of transmitter module optical efficiency and AOM diffraction efficiency (total 50%).	6
2.2 Schematic diagram of the real-time interferometer differential arm (DARM) control loop and calibration pipeline adopted from [4, 14].	7
3.1 KAGRA photon calibrator. The calibration system is placed around the EXA/EYA chamber. We mount the optical lever and optical baffle as well. The EXA/EYA chambers are placed at 36 m far from the ETM.	12
3.2 Stay free zone of the outside of the EXA/EYA chamber. All the com- ponents are placed at stay free region.	13
3.3 Transmitter module of KAGRA Pcal. We place the optical table on the triangle table. The readout and control device are housed into the legs of table.	14
3.4 Optical layout of KAGRA photon calibrator. The laser power is mod- ulated and controlled by the acousto-optic modulator (AOM). This modulated laser is sent to a 50:50 beam splitter, where we monitor the modulated laser power by using the integrating sphere.	15
3.5 The fiber laser and drawing of isolato. The module is placed under the Tx module [17].	15
3.6 Result of mode matching calculation from faber laser to AOM focus using JamMt [21].	18
3.7 Result of mode matching calculation from the AOM to the ETM focus using JamMt [21].	19
3.8 Result of mode matching calculation from AOM to photo detector fo- cus using JamMt [21].	19
3.9 The simulated HR coating on the fused silica mirror for 22.5 degree of incident angle [22].	20
3.10 The simulated HR coating on the fused silica mirror for 45 degree of incident angle [22].	21
3.11 Diagram of feedback loop for OFS.	23
3.12 Developed photo detector for KAGRA Pcal.	24
3.13 Fabricated cover.	25
3.14 The picture of photo detector. The diameter of photo detector is 3 mm. We control the incident power by changing diameter of the collimator and resistance of trans impedance amplifier	26
3.15 Circuit of photo detector designed by LIGO (D1300210-v4).	26
3.16 Periscope structure. We place the twelve 3-inch mirrors in total. The red and blue line correspond to lower and upper beam path, respec- tively. The upper and lower beams push the node point of the mirror surface.	28

3.17 Schematic view of periscope position. We optimized the periscope positions. We fix the separation of Tx module mirror, and each distance, L_{win} , L_{m1} , L_{m2} and L_{m3} . x is distance from the window.	28
3.18 Calculated separation of D_{win} , D_{m2} , and D_{m3} by changing the distance from the window. Blue, Green and Red curves are separation position on the window, MP2 and MP3. Purple dashed lines are incident angle of the laser to window. We find the optimal point at 355 mm point corresponding to 1.6 degree incident angle.	29
3.19 Simulated reflection of AR coating of one surface. We optimize the coating frequency at 1047 nm. This plot is provided by Sigma-koki.	30
3.20 View window with periscope. We mount the AR coated fused silica window on the ICF152 flange. The AR coating is optimized at 1047 nm. We mount the periscope at the vacuum side of the window. The incident angle of the periscope is 50 degrees.	30
3.21 Simulated deformation of Pcal window [28]. The center deformation is $0.85 \mu\text{m}$	31
3.22 Optical layout of receiver module. We mounted QPD for monitoring beam position drift. Total power of the laser is measured by the integrating sphere.	32
3.23 Mirror and Telephoto camera (TCam). We place the TCam on the structure. The image of ETM is referred by two mirrors. One mirror is mounted in vacuums. Another is placed at outside of chamber. The specification of mirrors are listed in Table. 3.15.	34
3.24 Moon light focuser.	34
3.25 Window design. We employ the AR coated fused silica window.	35
3.26 MEDM of KAGRA photon calibrator. The system is based on LIGO MEDM. We improve this system for BPM.	36
4.1 Fitting of z displacements, Δz_{DH} of the drumhead mode as a function of $r = \sqrt{x^2 + y^2}$ for LIGO case (left) and KAGRA case (right). The fitted node positions, r_{DH} , where $\Delta z_{DH} = 0$ are 109.0 mm and 65.3 mm for LIGO and KAGRA cases, respectively.	40
4.2 The z displacement, Δz_{BF} , for the butterfly mode as a function of $r = \sqrt{x^2 + y^2}$ and $\theta = \arctan(y/x)$ for the LIGO case. The KAGRA case show very similar behavior. The four node lines lie at $\theta = \pm 1/4\pi$ and $\pm 3/4\pi$	41
4.3 The ratio, $R(f)$ between the total sensed motion, $D_{\text{eff}(f)}$ and free mass motion, $D_{\text{free}}(f)$ as a function of frequency, f for optimally positoned beams and ± 2 mm and ± 4 mm offsets for (top) LIGO case and (bottom) KAGRA case. The cross check of the simulation is also done with COMSOL [34] and shown for optimum positoin and ± 2 mm offsets with open cross symbols.	43
4.4 The CAD model of the KAGRA ETM with flat cuts and ears.	44
4.5 Drumhead (top) and Butterfly (bottom) modes for KAGRA ETM.	45
4.6 Fitting of z displacements, Δz_{DH} of the drumhead mode as a function of y for KAGRA ETM model. The fitted dnode positions, r_{DH} , where $\Delta z_{DH} = 0$ are asymmetric and located at -66.5 mm and 62.7 mm.	46

4.7	The ratio between the total sensed motion and rigid body motion as a function of frequency for optimally positioned baams and ± 1 mm and ± 3 mm offsets. The cross check of the simulation is also done with COMSOL [34] and shown for optimum position and ± 1 mm offsets with open cross symbols.	46
5.1	KAGRA working standard.	48
5.2	comparison with GS and WS.	48
5.3	Voltmeter made by keithlay.	49
5.4	Calibration of end-station. We calibrate TxPD and RxPD using WSK. .	50
6.1	Image of beam position monitor. We will over-plot the estimated beam position on the picture.	54
6.2	Setup of demonstration test. We place the camera at 36m far from the ETM. This distance correspond to KAGRA configration.	55
6.3	Raw data of Image analysis (left picture). We are trimming the target region. The size of target is 24×24 mm.	55
6.4	Strategy of analysis. First we trim the data around the target. Second we convert to Gray scale. Third we set the threshold. Fourth, we pick up the data point using mask.	56
6.5	Fitting result of image analysis. Black dots are data points larger than threshold. We masked data around outer circle. Red circle is best fitting. .	57
7.1	Transmitter module with two AOM system.	60
7.2	Performance comparison of laser power standard system at 1064nm wavelength and 1W power in the national standard institutions in the world [35].	61
7.3	61
A.1	Transfer functions of DARM open loop gain and actuators assumed in this simulation.	66
A.2	Deformation of $R(f)$ due to the relative calibration bias on G_C	66
A.3	Deformation of $R(f)$ due to the relative calibration bias on f_C	67
A.4	Deformation of $R(f)$ due to the calibration bias on A_T	67
A.5	Comparisons of relative deformed (red solid lines) and fitted (blue dashed lines) wave forms with respect to the true one, in the three cases where G_C , f_C and A_T are biased by $\pm 10\%$, ± 30 deg., and $\pm 10\%$, respectively.	69
A.6	The systematic bias on the five source parameters as a function of variations of calibration parameters assuming the signal similar to GW150914 (left), and the extreme case where the GW150914 source is 200 Mpc away (right).	70

List of Tables

3.1	Specification summary of photon calibrator [5, 6, 13].	11
3.2	Specification summary of CW fiber Laser [17].	16
3.3	Specification of beam shutter [18].	17
3.4	Specification of HWP [19].	17
3.5	Specification of lenses [19].	20
3.6	Specification of Mirrors.	21
3.7	Specification of beam splitter [19].	22
3.8	Typical gain parameter of OFS.	23
3.9	Specification of AOM [24].	24
3.10	Specification of InGaAs detector.	25
3.11	Simulation parameter for ANSYS [28]	29
3.12	Specification of Mirrors in periscope.	31
3.13	Specification of Mirrors in Rx module.	32
3.14	Specification of QPD.	33
3.15	Specification of mirrors in camera	34
4.1	Simulation parameters and resuls for perfect cylinder studies.	40
4.2	Simulation parameters and resuls for the KAGRA ETM CAD model.	42
6.1	Fitting result of camera demonstration test.	56

Chapter 1

Introduction

1.1 Calibration of a Gravitational-Wave detector

KAGRA is a laser interferometer using four mirrors (test masses) suspended from multi-stage pendula to form two perpendicular optical cavities (arms). Gravitation Wave (GW) strain causes differential variations of the arm length and generates power fluctuations in the detector readout port. The power fluctuations measured by photodetectors work as the GW readout signal and an error signal to control the differential arm length. For the stable operation of the instrument, a feedback control of the differential arm length is required. This control is achieved by taking a digitized readout signal, applying a set of digital filters, and sending the control signal to the test mass actuators. Therefore, estimation of the equivalent GW strain sensed by the interferometer requires detailed characterization and correction for the feedback control loop.

The calibration uncertainties are directly translated to the systematic errors on the absolute GW signal amplitude. In case of LIGO GW150914 event, the calibration was established to an uncertainty (1σ) of less than 10% in amplitude and 10 degrees in phase [1]. In case of LIGO GW151226 event, the calibration uncertainty (1σ) in both detectors at the time of the signal is better than 8% in amplitude and 5 degrees in phase [2].

The primary impact of the calibration uncertainties to the physics parameters is the determination of the distance to the source. The 10% uncertainties of the GW amplitude directly correspond to 10% uncertainties on the estimation of the luminosity distance. Furthermore, since the estimation of the population of the GW sources depends on the third power of the source distance, 10% calibration uncertainties will be translated into $\sim 30\%$ uncertainties on the population estimation.

The calibration uncertainties also affect the coordinate reconstruction particularly in the case that only up to three detectors in the world GW detector network can detect the GW signal. This can often happen because the sensitivity of interferometer has directional dependence. The effect of calibration uncertainties is visible at high signal-to-noise ratio events where the angular resolution is less affected by the detector noise. In such cases, the pointing accuracy can get worse by factor of $2\sim 4$ with 10% calibration uncertainties [3].

1.2 Roles of the photon calibrator

Photon calibrators are the primary calibration tools in the Advanced LIGO and Advanced Virgo detectors [4–6]. Earlier versions have been tested on various interferometers [7–9], and they have evolved significantly in LIGO over the past ten years [10]. There are several unique roles required to the photon calibrator:

1. Check of the sign of $h(t)$

Since the direction of the movement of test mass is proportional to the laser power, photon calibrator allows a direct check of the sign of the reconstructed $h(t)$ channel compared to the definition taken in agreement with other experiments. In initial phase of Virgo, the primary purpose of photon calibrator was to check the sign of $h(t)$ [11].

2. Calibration during the observing periods

Calibration methods without using photon calibrator such as using radio-frequency oscillator and laser wavelength can be done only under the limited condition where the interferometer is not operating in the optimum sensitivity. The propagation of calibration parameters from the high noise condition to the low noise condition can introduce additional unknown source of systematic errors. On the other hand, the photon calibrator is a completely independent instrument of the interferometer and therefore can actuate the test masses during the observation periods with optimum sensitivity.

3. Independence of calibration method

and reliability assurance of interferometer

Injecting calibration signals into the control feedback loop has a limitation to reduce the systematic errors because it is calibrating the loop itself. Without Pcal, it is difficult to disentangle each uncertainty inside the loop, such as optical gain and actuator efficiency. On the other hand, Pcal has a strong advantage to enable to inject calibration signals independent of the control loop and provide an additional way to reduce the systematic uncertainties.

4. Globalization of the calibration

It is necessary to calibrate and compare the absolute accuracies of KAGRA, LIGO and Virgo, or at least we need to have a way to evaluate the difference of absolute GW amplitude between different detectors. This kind of difference introduces bias on the physics parameters such as the source localization. Typical examples are cosmic-ray air shower observations and X-ray observations. In the long history of the air shower experiments, there have been always discussions about the absolute energy estimation. On the other hand, X-ray detector can be calibrated by the radio isotope sources and there is no question raised. In the GW experiment, absolute calibration is a difficult work but therefore it will be the key issue of the experimental verifications in the next decades.

1.3 Schedule of KAGRA

In order to coincide the observation plan by LIGO and Virgo [12], KAGRA is currently installing the instrument to meet the following observation schedule [13]:

1. Phase-1: 2017.3 – 2018.3

Operation of Michelson interferometer in cryogenic condition followed by introducing Fabry Pérot cavity.

2. Phase-2: 2018.4 – 2019.3 (Opening)
Full lock of RSE (Resonant Sideband Extraction)
3. Phase-3: 2019.4 – 2020.3 (Early)
One year commissioning after the first full operation, then improve the sensitivities to achieve the design goal
4. 2020 – 2021: Middle term observation
5. 2021 – 2022: Late term observation
6. 2022 – : Observation with the designed sensitivity

1.4 Calibration requirements from data analysis

A calibration accuracy will decide how precise scientific results can be extracted from various data analysis of gravitational wave events. We have to consider the error propagation not only from calibration accuracy to the reconstructed strain data both in time series $h(t)$ and frequency domain $h(f)$, but also from $h(t)$ and $h(f)$ to many cases of event analysis. However, parameter estimations in GW event data analysis now is not simple, e.g. employing Markov-chain Monte Carlo, Bayesian Estimation, higher-order waveforms, numerical simulated waveforms, etc. It is not so easy to conclude the requirement of the accuracy of calibration immediately. There are some challenges to estimate them in actual situation now. Here, we would like to introduce some typical cases of errors in event analysis. The calibration errors will be serious in high signal-to-noise ratio (S/N) events, but also effective on statistical estimation with many events.

One of the cases which can image the situation simply is parameter estimation of compact binary coalescence. If the 5% amplitudes error of GW reflects as 5% error on the distance estimation of the binary directly. For each event with low S/N (typically S/N~10), the errors are dominated by detector noises. However, when we discuss with 100 or more events, we may found the effects of calibration errors. For example, neutron stars/black-holes binary merger rate estimation may have 15% biases with 5% biased $h(t)$. Or in cases of the events almost detection range (as like a few 100 Mpc for neutron star binary, several 100 Mpc ~ 1 Gpc for black-hole binary), 5% distance errors will be comparable with the correction of cosmological redshift. If we would like to discuss the population of binaries, to do the geometrical test of universe expansion, the calibration accuracy be necessary as 1% or less.

In the cases of multi-detector coincidence/coherence analysis are more serious on ‘absolute’ calibration. When we compare the waveforms from a few detectors, the errors on the waveforms from each detector might make biases on the results. For example, the direction guess will be slightly sifted to the azimuthal direction of the detector which have larger amplitude. The inference of polarization and inclination angle may have biases. The propagation is complex, because the number of parameters of compact binary stars are not small, at least nine without spin parameters. Similar biases will appear in stochastic GW analysis including radiometry.

Phase errors are also serious in multi-detector analysis. In compact binary case, phase errors of waveforms may cause errors on arrival time and mass of stars. An arrival time error propagates immediately on an inference of the source direction. Mass accuracy will reflect on the distance guess. In case of burst waves, we need to analyze waveform coherence. It will make biases more seriously, because that the

burst analysis has to treat the waveforms without certain analytic template waveforms by theory. It is well known that the phase error of the calibration will be large around the unity gain frequency, and such frequency is good sensitivity band in general. Therefore, it is very important to achieve the absolute calibration, that can be compared inter-observatories: LIGO, Virgo, KAGRA.

After the discovery of heavy black-hole binary GW150914, the science at the formation of larger black-hole after merging is attracting many people. Because, the black-hole physics will be possible at black-hole formation. Typical proposal is an analysis of the quasi-normal mode oscillation. When we extract the accurate waveform of ring-down gravitational waveform, it makes us possible to test the general relativity (GR). However, such accurate GR testing requires high S/N, because that the expected anomaly from GR is not so large. There is also another proposal of searching for ‘echo’ waves from black-hole. In these cases, we need ‘gold-plated’ events of high S/N larger than 30 or as like. These events are rare, however, approximately 2% of events selected $S/N > 8$ will have $S/N > 30$, i.e. we may get a few events of $S/N > 30$ in whole of 100 events. In this high S/N events, the accuracy of calibration will be dominant factor of waveform study. We need high-fidelity of waveform for gold-plated events. Even such events are small numbers of, but these have impact on advanced feature of physics.

In the KAGRA observational era, we have to assume above situations : multiple detector observation, a few or several 100 events, and a few gold-plated events.

Chapter 2

Photon calibrator

2.1 Photon calibrator

Photon calibrator relies on photon radiation pressure from auxiliary power-modulated laser beams reflecting on the test mass to apply periodic forces via the recoil of photons. Controlling and measuring the laser power accurately is one of the principal challenges of Pcal development. The KAGRA Pcal system consists of transmitter module, in-vacuum periscope, Receiver module and Beam monitor system. The transmitter module accurately modulates the beam power with internal feedback loop called optical follower servo. Two laser beams from the transmitter module enter the vacuum enclosure and relayed by mirrors mounted to a periscope structure located inside the vacuum envelope, then impinge on the test mass mirror to apply forces. The reflected beams are relayed exactly in the symmetric path by the other set of mirrors mounted to the periscope and enter the receiver module. Capturing the beams reflected from the test mass is important to ensure that the applied power is exactly same as modulated without losing somewhere in the beam path.

An important aspect of the performance of the Pcal system is the locations of the beam spots on the test mass surface. The photon pressure forces can induce both local and bulk elastic deformations of the test mass which compromise the accuracy of the calibration. To minimize the impact of these deformations, Pcal uses two beams displaced symmetrically from the center of the face of the test mass mirror. In order to determine and adjust the positions of the Pcal beams, the beam position monitor system will be installed. It consists of remote-controlled digital camera, telescope and relay mirrors. It will also provide monitoring of the surface condition of the test mass mirror as well as the change of the test mass mirror position during the cooling down phase.

The absolute displacement is described as

$$dx = \frac{2P \cos \theta}{c} s(f) \left(1 + \frac{M}{I} \vec{a} \cdot \vec{b} \right), \quad (2.1)$$

where P is an absolute power of the laser, c is the speed of light, θ is an incident angle of the laser, I and M are moment of inertia and mass of test mass, \vec{a} and \vec{b} is position vector of photon calibrator lasers and interferometer laser. Then, $s(f)$ is transfer function of the test masses. We assumed the masses, shapes and Young's modules of the each pendulum mass and fiber. According to transfer function, we can regard the motion of high frequency as free mass due to higher than the natural frequency. Therefore, we are able to assume as follows:

$$s(f) = \frac{1}{M\omega^2}, \quad (2.2)$$

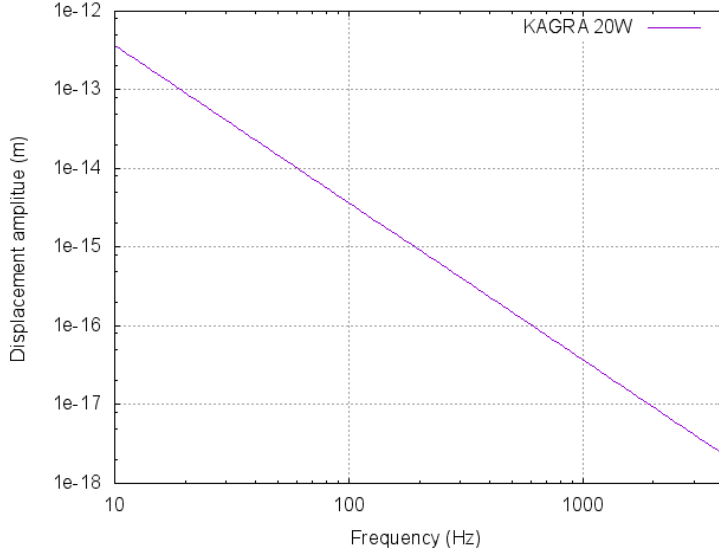


FIGURE 2.1: Frequency dependence of maximum displacement by KAGRA Pcal. Assumption 1: Using total laser power to one frequency. Assumption 2: pessimistic estimation of transmitter module optical efficiency and AOM diffraction efficiency (total 50%).

where ω is the angular frequency of test mass.

Using the KAGRA Photon calibrator parameters, which are listed in Table 3.1, we estimated the frequency dependence of maximum displacement in case of using full laser power to one frequency. Figure 2.1 is the result. In this calculation, we assume the 25% of total laser power can use for mirror displacement, 1/2 is caused by injecting waveform plus-minus, and remaining 1/2 is caused by pessimistic investigation of transmitter module optical efficiency(98.5% in LIGO) and AOM diffraction efficiency(96% in LIGO). The maximum displacement for each frequency can be written by

$$3.7 \times 10^{-11} / f^2 [\text{m}] \quad (2.3)$$

2.2 Purpose of photon calibrator

2.2.1 Interferometer Calibration

One of the main calibration method to reconstruct ΔL_{ext} , differential arm length (DARM), uses the combination of obtained error signal(d_{err}) and feedback signal(d_{ctrl}) with considering the slow temporal variations in aLIGO [4, 14]. In this document, we assume the LIGO DARM control system which is shown in Figure 2.2. This servo is described in term of (i) sensing function, $C(f, t)$ (ii) digital filters, $D(f)$ (iii)actuation function, $A(f, t)$, and $G(f, t) = C(f, t)D(f)A(f, t)$ is the DARM open loop transfer function

The sensing function $C(f, t)$ can be written in

$$C(f, t) = \frac{\kappa_C(t)}{1 + i f / f_C(t)} Q(f) \equiv P(f, t)Q(f). \quad (2.4)$$

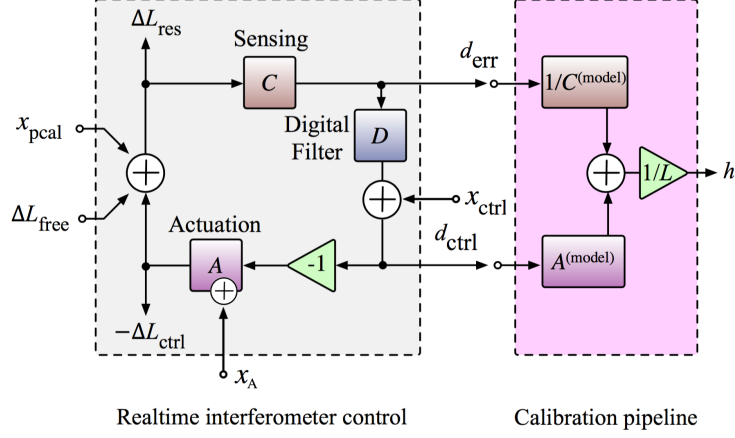


FIGURE 2.2: Schematic diagram of the real-time interferometer differential arm (DARM) control loop and calibration pipeline adopted from [4, 14].

$Q(f)$ is the time-independent part of the sensing function, which includes photodetector response, electronic response and signal delay caused by light traveling time of interferometer arm. $P(f, t)$ is the time-dependent part of the sensing function, which includes optical gain sale factor, $\kappa_C(t)$ and coupled-cavity response. Coupled-cavity response is approximated by a single pole ($f_C(t)$).

The actuation function $A(f, t)$ can be written in

$$A(f, t) = \kappa_{PU}(t)(A_{P,0}(f) + A_{U,0}(f)) + \kappa_T(t)A_{T,0}(f). \quad (2.5)$$

$A_{P,0}(f)$, $A_{U,0}(f)$ and $A_{T,0}(f)$ are models of the actuation function of the penultimate, upper-intermediate and the test mass stage when both $\kappa_{PU}(t_0)$ and $\kappa_T(t_0)$ are set to 1.

To monitor those four time variation parameters, $\kappa_C(t)$, $f_C(t)$, $\kappa_{PU}(t)$ and $\kappa_T(t)$, we need to inject modulated excitations into the DARM loop. Also, to measure the $\kappa_C(t)$ individually form $\kappa_{PU}(t)$ and $\kappa_T(t)$, we need additional system to inject modulated excitations to ETM. Photon calibrator is powerful tool for this purpose. So, we should inject following four modulated excitations; (i) two modulated excitations using a photon calibrator system (x_{pcal1} and x_{pcal2}) (ii) one modulated excitations into the overall DARM actuation (x_{ctrl}) (iii) one modulated excitations into the test mass stage actuation (x_T). The responses in d_{err} at time $t = t'$ for each modulated excitations can be written by

$$d_{err,t'}(f_{pcal1}) = \frac{C(f_{pcal1}, t')}{1 + G(f_{pcal1}, t')} x_{pcal1} \quad (2.6)$$

$$d_{err,t'}(f_{pcal2}) = \frac{C(f_{pcal2}, t')}{1 + G(f_{pcal2}, t')} x_{pcal2} \quad (2.7)$$

$$d_{err,t'}(f_{ctrl}) = \frac{-A(f_{ctrl}, t')C(f_{ctrl}, t')}{1 + G(f_{ctrl}, t')} x_{ctrl} \quad (2.8)$$

$$d_{err,t'}(f_T) = \frac{\kappa_T(t')A_{T,0}(f_T, t')C(f_T, t')}{1 + G(f_T, t')} x_T \quad (2.9)$$

Using x_{pcal1} and x_T modulated excitations, $\kappa_T(t')$ is obtained. Using x_{ctrl} modulated excitation and $\kappa_T(t')$, $\kappa_{PU}(t')$ and $A(f, t')$ are obtained. Using x_{pcal2} modulated

excitation and $A(f, t')$, $\kappa_C(t')$ and $f_C(t')$ are obtained.

Finally, $\Delta L_{\text{ext}}(t)$ is reconstructed by following equation:

$$\begin{aligned}\Delta L_{\text{ext}}(t) = & [\mathcal{P}(f_C(t))/\kappa_C(t) * \mathcal{Q}]^{-1} * d_{\text{err}}(t) \\ & + [\kappa_{PU}(t)(\mathcal{A}_{P,0} + \mathcal{A}_{U,0}) + \kappa_T(t)\mathcal{A}_{T,0}] * d_{\text{ctrl}}(t),\end{aligned}\quad (2.10)$$

where $\mathcal{P}(f_C(t))$, \mathcal{Q} , $\mathcal{A}_{P,0}$, $\mathcal{A}_{U,0}$ and $\mathcal{A}_{T,0}$ are the time-domain filters created from $P(f, t)$, $Q(f)$, $A_{P,0}(f)$, $A_{U,0}(f)$ and $A_{T,0}(f)$, and $*$ denotes convolution.

To reduced the systematic uncertainty, frequencies of modulated excitations are selected with following conditions: (1) Frequencies of x_{pcal1} , x_{ctrl} and x_T should be in a narrow frequency band. (2) Such frequency band should be selected where the magnitude of the transfer functions of the combined penultimate and upper intermediate mass stage and the test mass stage are approximately equal. (3) Frequencies of x_{pcal2} should be near the coupled-cavity pole frequency.

2.2.2 Hardware injection test

Hardware injection test is one of the important end-to-end test which inject various waveforms to end test mass. To analyze the hardware injection test data, we perform detector performance, data acquisition system, calibration system, data transfer system, data analysis pipeline. We can obtain the waveforms with detector response, so various information will be obtained through hardware injection test.

- test of calibration system

We can test the strain signal calibration accuracy of sign, amplitude, phase and timing.

- check of analysis tools

To inject the gravitational wave signals such as inspiral signal from compact binary coalescence, we can check the analysis tools/pipeline and systematic error due to calibration accuracy.

- injection of complex signals

To inject complex signals such as supernovae waveform, Cosmic string waveform, ringdown waveform, we can judge that complex signals can observe correctly or not. If we understood that there are un-observable signal, we can consider the update of observation scenario or calibration system.

- blind injection

When we apply hardware injection test, it will be better to inject signal without DARM control loop. Ensure that there is no mistake (mis-understandings) in injection test when we check and confirm the calibration system. In case of that there are two mis-understandings in injection test and calibration system, we sometimes miss those mis-understandings due to counteract each other. Reducing the systematic uncertainty especially for injection system is crucial. Injection test itself is possible without photon calibrator, but there are advantages to have injection test with photon calibrator

1. Injection test by photon calibrator is simpler than other injection system

2. We can injection test outside of DAEM main loop

The counteract by two-misunderstanding can be reduced in photon calibrator.
But we should take into account common system, such as DAC/AI filters

3. Inject signals without considering feedback signals

We don't need to consider the saturation in DAC, and the advantage of larger amplitude injection because we don't take into account fluctuation of feedback signals.

4. Dis-advantage of photon calibrator.

We didn't establish the cross check of photon calibrator injection completely. There are mis-matching between photon calibrator and other injection methods. Multiple approach of injection test will be important for the future calibration/injection tests.

2.2.3 Photon pressure actuator

2.3 Calibration line of KAGRA

At least one PCAL calibration line is needed as a standard candle for the DARM actuator calibration, and another line for each of the suspension stages that will be used for DARM actuation. In case of LIGO it has been made to do thus far with 1/2 as many lines as interferometer response parameters to intend to track, because one can use the amplitude and phase for each line to obtain two parameters. If we need to track the optical gain and coupled cavity pole frequency (without Signal Recycling Cavity (SRC) detuning) then we will need one line. If we need to track those as well as the SRC detuning spring frequency and factor Q, we will need 2 lines.

In the O1/O2 phase of LIGO, the interferometer configuration is made without SRC detuning, or called Extreme Resonant Sideband Extraction (ERSE) where the microscopic SRC phase is 90 deg. In this case, the optomechanical response can be approximated by a single pole,

$$C_{ERSE}(f) = \frac{g}{1 + if/p} \quad (2.11)$$

Where f is the frequency, g is the optical gain, and p is coupled cavity pole frequency, $p = f_a \times (1 + r_s)/(1 - r_s) = 365$ Hz. In case of LIGO, $f_a = cT_i/8\pi L = 42$ Hz and $r_s = \sqrt{1 - T_s}$ with transmissivity of Input Test Mass (ITM) and Signal Recycling Mirror (SRM) as $T_i = 0.014$ and $T_s = 0.37$ [15].

In case of KAGRA, the design values of $T_i = 0.004$ and $T_s = 0.1536$ give the coupled cavity pole frequency $p = 387$ Hz. One calibration line around this frequency should be added to track the optical gain and the cavity pole frequency.

As discussed in Section 2.2.1, we need at least four calibration line with following characteristics:

1. two pcal calibration line ($x_{pcal1,2}$) with ~35Hz and ~330Hz.
2. one calibration line to feedback signal (x_{ctrl}) with ~35Hz.
3. one calibration line to end test mass (x_T) with ~35Hz.

More, to monitor the calibration accuracy and open loop transfer function, it will be better to add at least four calibration line (two for pcal and two for feedback), frequencies will be $\sim 100\text{Hz}$ and $\sim 1000\text{Hz}$.

The total laser power with photon calibration can be calculated by following equation

$$P_{\text{laser}} = \sum_i \sqrt{2} L S_n(f_i) \frac{1}{4} \frac{\text{SNR}(f_i)}{\sqrt{T}} \frac{Mc(2\pi f_i)^2}{2 \cos \theta}, \quad (2.12)$$

where f_i is i-th calibration line frequency, L is arm length, $S_n(f_i)$ is sensitivity curve [strain(rms)/rHz], $\sqrt{2}$ corresponds to conversion coefficients from peak value to effective value, $\text{SNR}(f_i)$ is required signal to noise ratio, T_i is length of fourier transform, M is mirror mass, c is light speed.

Chapter 3

Instruments descriptions

3.1 Layout of Photon calibrator

The KAGRA photon calibrator is placed around EXA/EYA chamber, which is installed 36 m away from the end test mass (ETM). We push the mirror surface with the modulated photon pressure directly. Figure 3.1 shows the layout of the KAGRA photon calibrator. The photon calibrator consists of transmitter module (Tx module), receiver module (Rx module), periscope, and telephoto camera module (TCam module). We place the 20 W laser in Tx module, whose frequency is 1047 nm. The 1064 nm laser is not used due to avoid the coupling with main beams. The power of the laser is modulated by the optical follower servo (OFS). We split the beams in Tx module for pushing the drum head node points of the ETM due to elastic deformation. We transfer the beams to the ETM though the periscope. All the periscope structures are placed into the EXA/EYA chamber. The beam is received by the Rx module. We place a 6 inches integrating sphere for the accurate measurement of the laser power and two quadrant photo detector (QPD) for the beam position monitor. We also measure the beam position on the ETM surface using the telephoto camera (TCam). The Tcam is consists of the astronomical telescope, focuser, and high resolution digital camera. The specification summary of KAGRA photon calibrator is shown in Tabel. 3.1. Details of instruments are described following section.

3.2 Placement of modules

The modules are placed around the EXA/EYA chamber. We need to pay attention to conflict with other components, such as optical lever stage, walls of the tunnel, doors of the chamber and working space. Figure. ?? shows the stay free regions around the

TABLE 3.1: Specification summary of photon calibrator [5, 6, 13].

	KAGRA	advanced LIGO	advanced Virgo
Mirror material	Sapphire	Silica	Silica
Mirror mass	23 kg	40 kg	40 kg
Mirror diameter	220 mm	340 mm	350 mm
Mirror thickness	150 mm	200 mm	200 mm
Distance of Pcal from ETM	36 m	8 m	1.5 m
Pcal laser power	20 W	2W	3 W
Laser frequency	1047 nm	1047 nm	1047 nm
Incident angle	0.72 deg	8.75 deg	30 deg

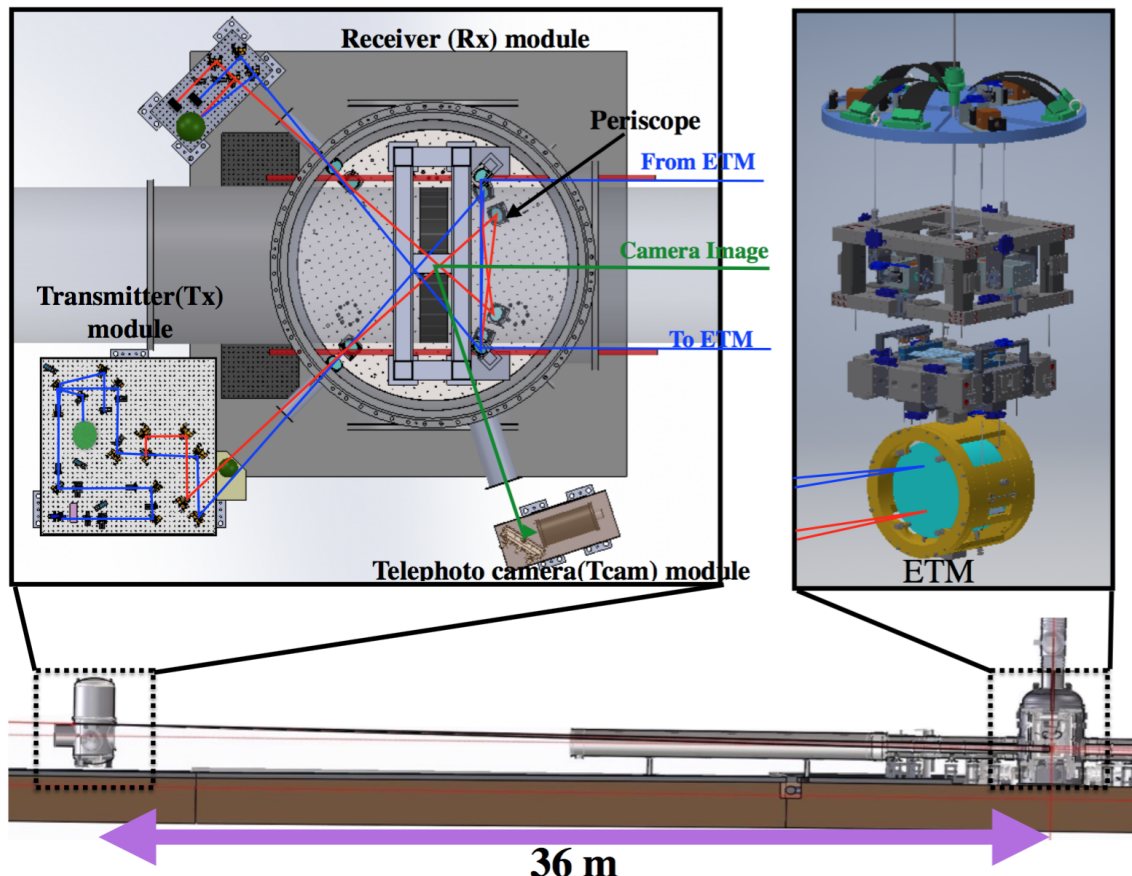


FIGURE 3.1: KAGRA photon calibrator. The calibration system is placed around the EXA/EYA chamber. We mount the optical lever and optical baffle as well. The EXA/EYA chambers are placed at 36 m far from the ETM.

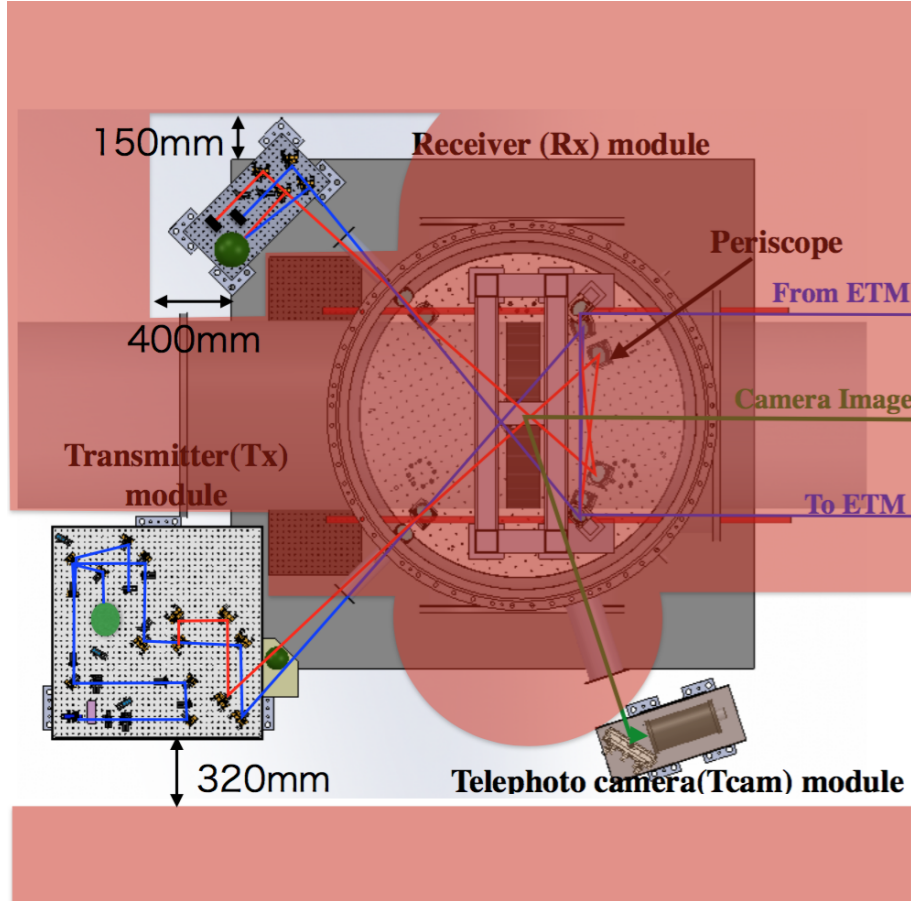


FIGURE 3.2: Stay free zone of the outside of the EXA/EYA chamber.
All the components are placed at stay free region.

EXA/EYA chamber. We need to avoid the red regions for mounting modules. All the modules meet our requirements.

3.3 Transmitter (Tx) module

The Tx module is placed at the side of the EXA/EYA chamber. Figure 3.3 shows the view of Transmitter module. All the optical components are mounted on the 900 mm × 900 mm breadboard (B9090L; Thorlabs) [16]. The bread board is placed on the support structure. The electrical module for the control and readout are also hosed in the support structure.

Figure 3.4 shows the optical layout of Tx module.

3.3.1 Fiber laser

We employ the CW fiber laser made by the LER photonics as shown in Fig. 3.5. The maximum power and frequency are 20 W and 1047 nm, respectively. The model number of the laser is CYFL-TERA-20-LP-1047-AM1-RGO-OM1-T305-C1 [17]. The maximum laser power of KAGRA Pcal is 10 times larger than that of LIGO. This is because that we need the high power laser for the injection test and photon pressure actuator technique. The typical beam width of the laser is 0.25 mm when we mount the isolator. We summarize the specification of the laser as shown in Table 3.2.

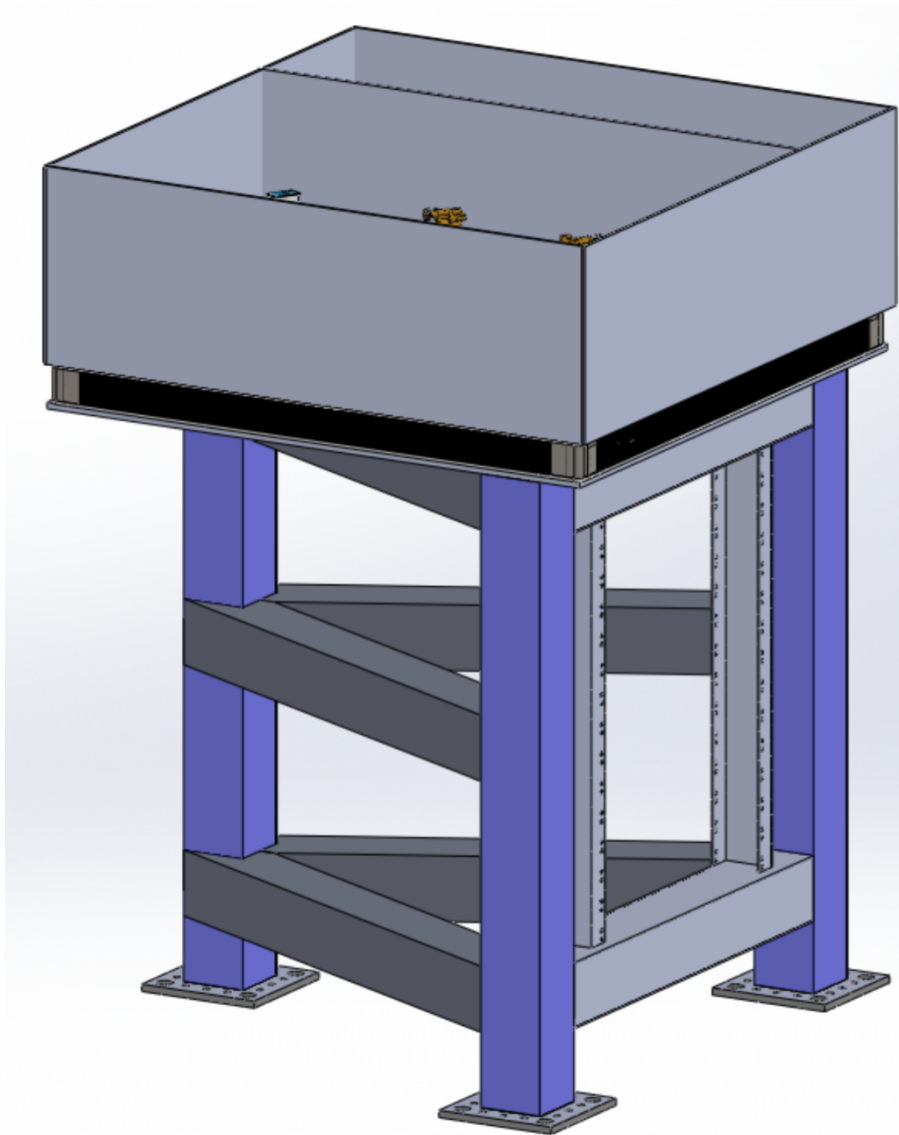


FIGURE 3.3: Transmitter module of KAGRA Pcal. We place the optical table on the triangle table. The readout and control device are housed into the legs of table.

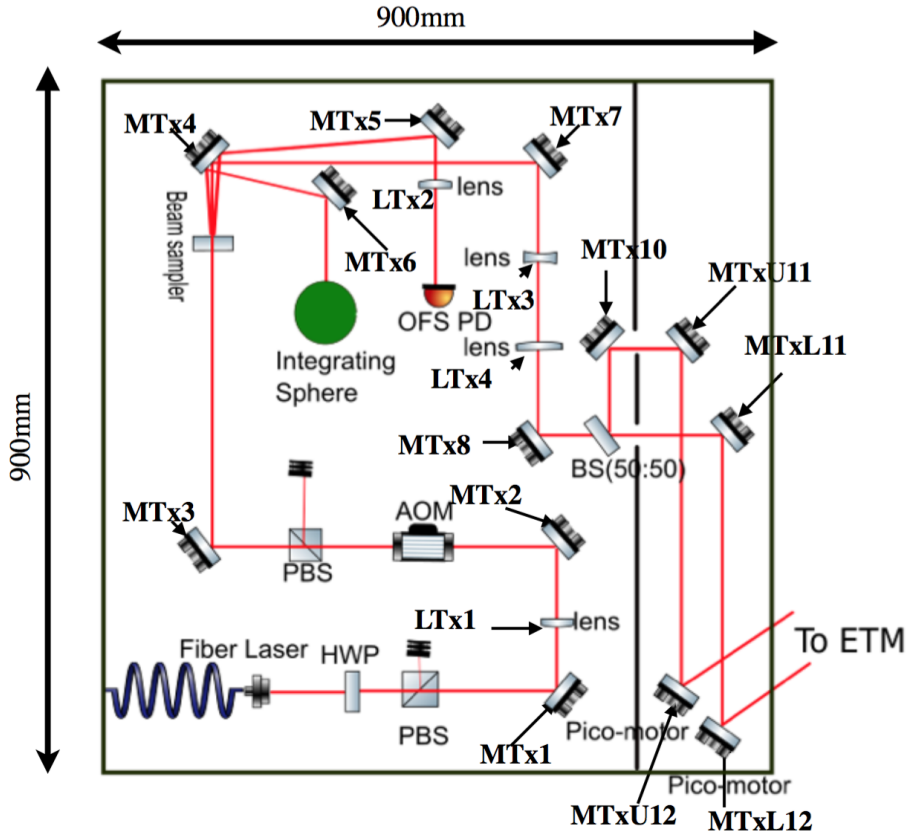


FIGURE 3.4: Optical layout of KAGRA photon calibrator. The laser power is modulated and controlled by the acousto-optic modulator (AOM). This modulated laser is sent to a 50:50 beam splitter, where we monitor the modulated laser power by using the integrating sphere.

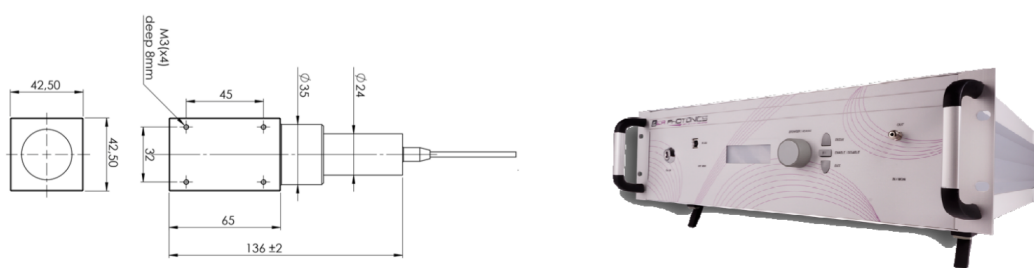


FIGURE 3.5: The fiber laser and drawing of isolato. The module is placed under the Tx module [17].

TABLE 3.2: Specification summary of CW fiber Laser [17].

Characteristic	Typical value	Unit	Note
Operating central wavelength	1047	nm	± 1 nm
CW output power	20	W	
Output signal line-width	0.5	nm	FWHM
Output power stability	± 1	%RMS	Output power: 20 W
Output power tunability	10-100	%	
Optical polarization	Linier		
Polarization extinction ratio	15	dB	
Output fiber	PLMAFUD3460		Nufurn company
Output fiber length	2	m	
Beam diameter	0.5	mm	with isolator
Beam quality	1.1	M^2	
Control mode	Active current control, Active power control		
Beam quality	1.1	M^2	
Supply voltage	84-264	V	AC 47 to 63 Hz
Power consumption	650	W	
Housing	448x451x132.5	mm	
Total weight	13	kg	
Cooling	Air cooled with fans		
Operating temperature	15-35		
Humidity	5-85	%	

TABLE 3.3: Specification of beam shutter [18].

Characteristic	Typical value	Unit	Note
Max laser power	20	W	
Aperture size	15	mm	
Drive voltage	11-14	V DC	
Current consumption	150	mA	
Size	98 × 63.5 × 36	mm	

TABLE 3.4: Specification of HWP [19].

Characteristic	Typical value	Unit	Note
Waveplate Type	Quartz Waveplates		
Wavelength Range	1047	nm	
Retardance	$\lambda/2$		
Clear Aperture	85	%	of diameter
Reflection	0.25	%	
Retardance Tolerance	$\lambda/200$ to $\lambda/500$		at 23Degree C
Material	Crystal Quartz		
Surface Quality	10-5	scratch-dig	
Waveplate Diameter	12.7	mm	

3.3.2 Beam shutter

We have to pay attention to safety for the operation of the high power laser. In order to dump the beam, we use the beam shutter made by lasermet company [18]. The model number of the shutter is LS-10-12. The aperture size and maximum laser power are 15 mm and 20 W. These number meet our requirement due to the laser spot size and maximum power. We control the beam shutter on the MEDM as shown in Sec. 3.7. The specification of the beam shutter is shown in Table. 3.3.

3.3.3 Zeroth order half wave plate

To control the polarization angle of the incident beam, we employ the zeroth order half wave plate (HWP) made by the CVI laser optics [19]. The model number of the HWP is QWPO-1047-05-2-R10 whose diameter is 12.7 mm. The HWP is mounted on the rotation mount made by Thorlabs. The thickness are optimized at 1047 nm. The specification of the HWP is listed in Table 3.4.

3.3.4 Polarizer

We place two polarizers to define the polarization angle accurately. This is because that the power of the laser is modulated by acousto-optic modulator (AOM) whose performance depend on the incident polarization angle. One polarizer is placed behind HWP. Another one is placed after AOM. The polarizer is made by Karl-Lamrecht [20]. We purchased TFPC12-1047 that is optimized at 1047 nm.

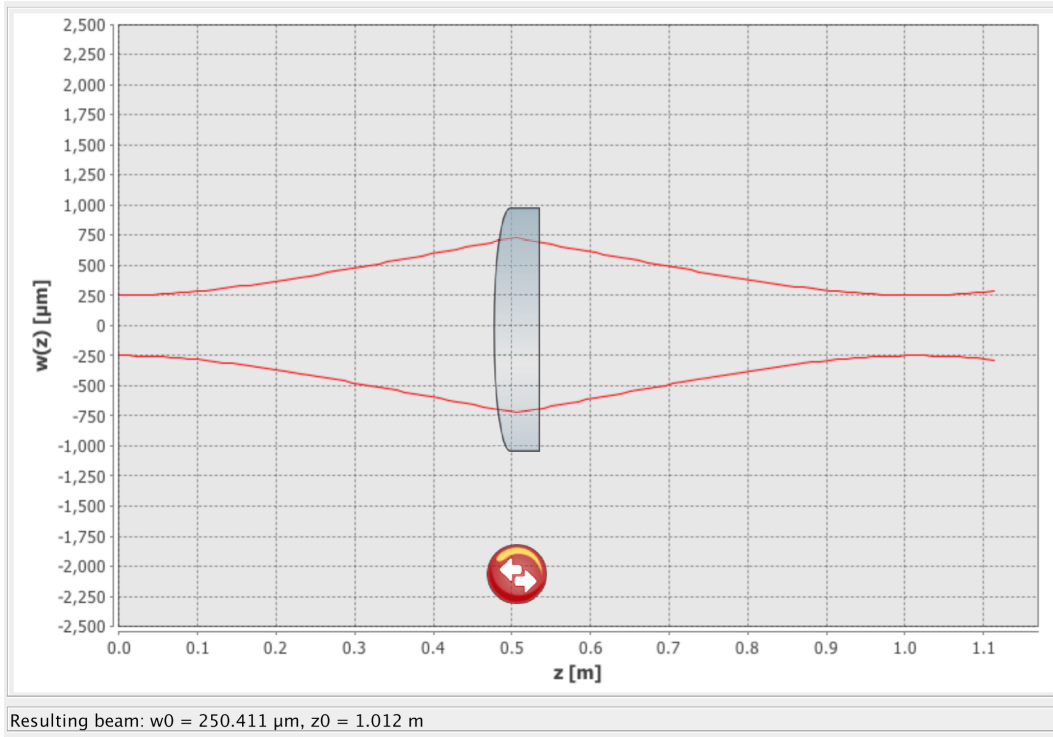


FIGURE 3.6: Result of mode matching calculation from faber laser to AOM focus using JamMt [21].

3.3.5 Lens

We have done a mode matching simulation using JamMt [21]. We assumed laser beam to be gaussian distribution. We have to place the focus of the laser at the AOM. Thus, we decide the optimal position and focal length of the 1 inch lens (LTx1), where the assumed beam waist of the fiber laser and AOM are 0.25 mm, respectively. The estimated beam spot size and lens position are shown in Fig. 3.6.

Furthermore, we place two lenses for placing the focus at the surface of the ETM. We employ the combination of 1 inch negative lens (LTx3) and 2 inch positive lens(LTx4). The Gaussian beam can describe the following relation:

$$w(z) = w_0 \sqrt{1 + \left(\frac{\lambda z}{\pi w_0^2} \right)^2}, \quad (3.1)$$

where λ is wavelength of the laser, w_0 is beam waist, z is direction from the focus. We estimate the minimum differential beam spot by changing beam waist because it make the alignment easier. The minimum beam spot is written by

$$\left. \frac{dw(z)}{dw_0} \right|_{z=36 \text{ m}} = 0. \quad (3.2)$$

The estimated beam spot is 5.5 mm at Tx module with 3.5 mm beam waist as shown in Fig. 3.7.

We also place the 1 inch lens (LTx2) at the front of the photo detector for the OFS. The calculated spot size is shown in Fig. 3.8. The beam width at the detector is 1000 μm which is less than clear aperture of detector (3 mm). The parameters of the

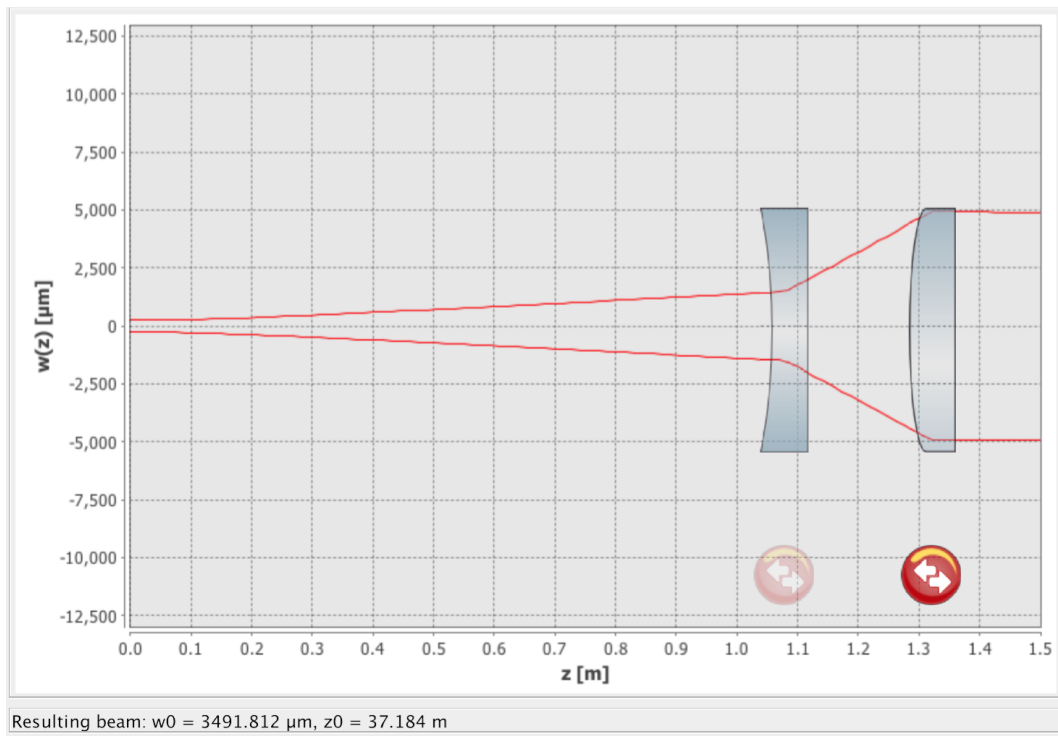


FIGURE 3.7: Result of mode matching calculation from the AOM to the ETM focus using JamMt [21].

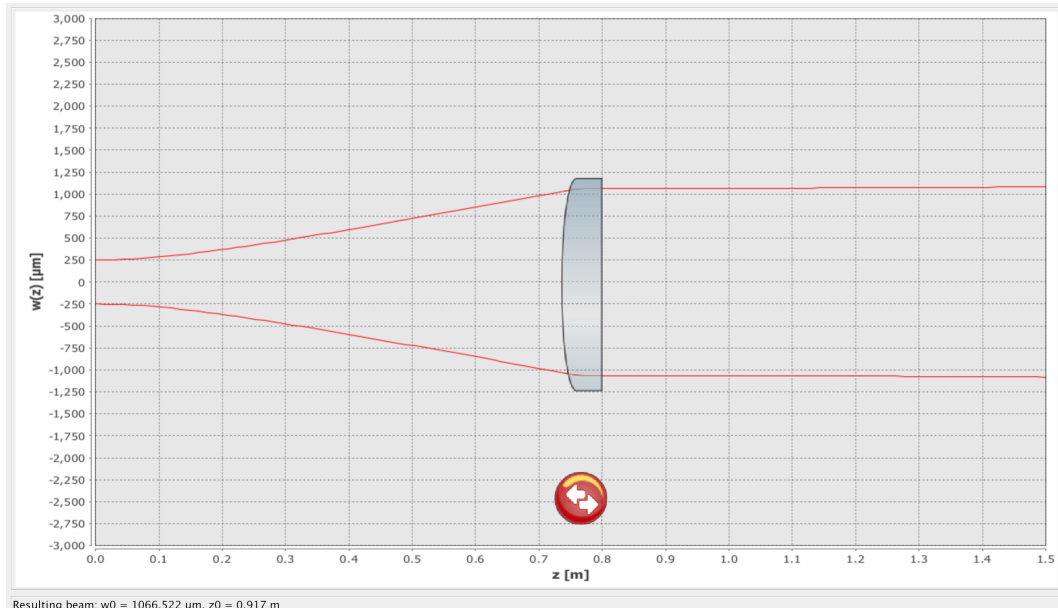


FIGURE 3.8: Result of mode matching calculation from AOM to photo detector focus using JamMt [21].

TABLE 3.5: Specification of lenses [19].

Lens number	part number	Diameter [mm]	Focal length (mm)	z (mm)	w
LTx1	PLCX250UV (CVI laser optics)	25.4	286.457	507	
LTx2	PLCX250UV (CVI laser optics)	25.4	801.991	768	
LTx3	PLCC100UV (CVI laser optics)	25.4	-114.538	1080	
LTx4	PLCX300UV (CVI laser optics)	50.8	343.615	1323	

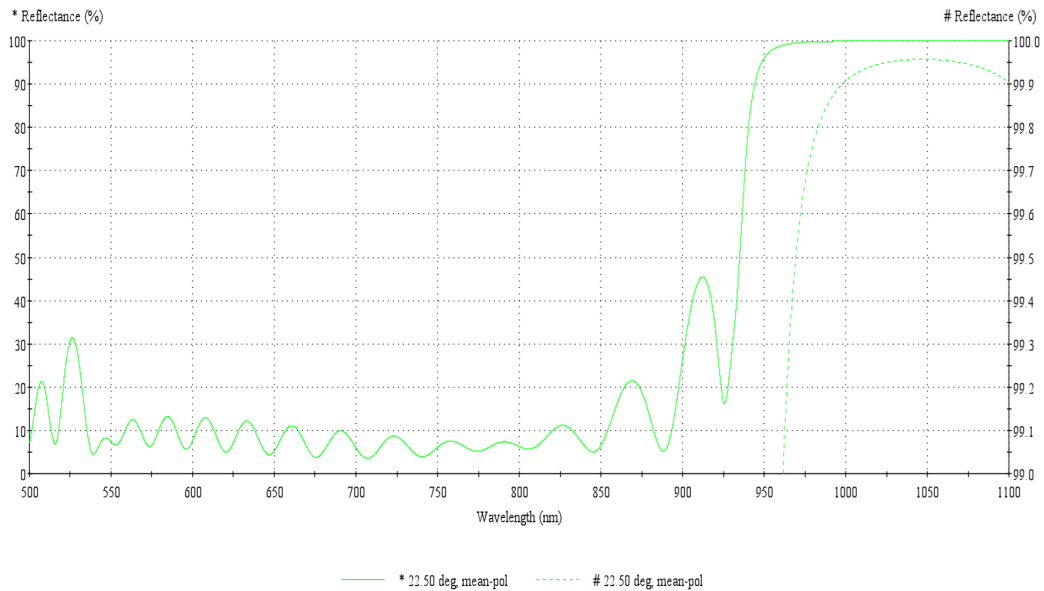


FIGURE 3.9: The simulated HR coating on the fused silica mirror for 22.5 degree of incident angle [22].

simulation results are listed in Table. 3.5. All lenses are made by CVI laser optics [19]. The material of lenses are fused silica. The AR coating are placed on both surface.

3.3.6 Mirror

We employ nine 1 inch mirrors and four 2 inch mirrors. The 1 inch mirror is made by CVI laser optics [19]. They place the HR coating on the surface of mirror. On the other hand, we use the HR coating on the fused silica disc of 2 inch in diameter. The coating and polishing the fused silica are made by Sigma-koki corporation [22]. The reflectances of the mirrors with 22.5 deg and 45 deg are shown in Fig. 3.9 and Fig. 3.10. The reflectance of the HR coating depends on the incident angle and the polarization angle. We labeled mirrors as shown in Fig. 3.4. The specification of mirrors are summarized in Table. 3.6. All mirror is aligned with optical mirror mount made by Newport company.

3.3.7 Optical mount with Pico-motor

The uncertainty of the beam position on the ETM is one of the largest systematic errors. To control the beam position, we employ the Pico-motor for changing mirror

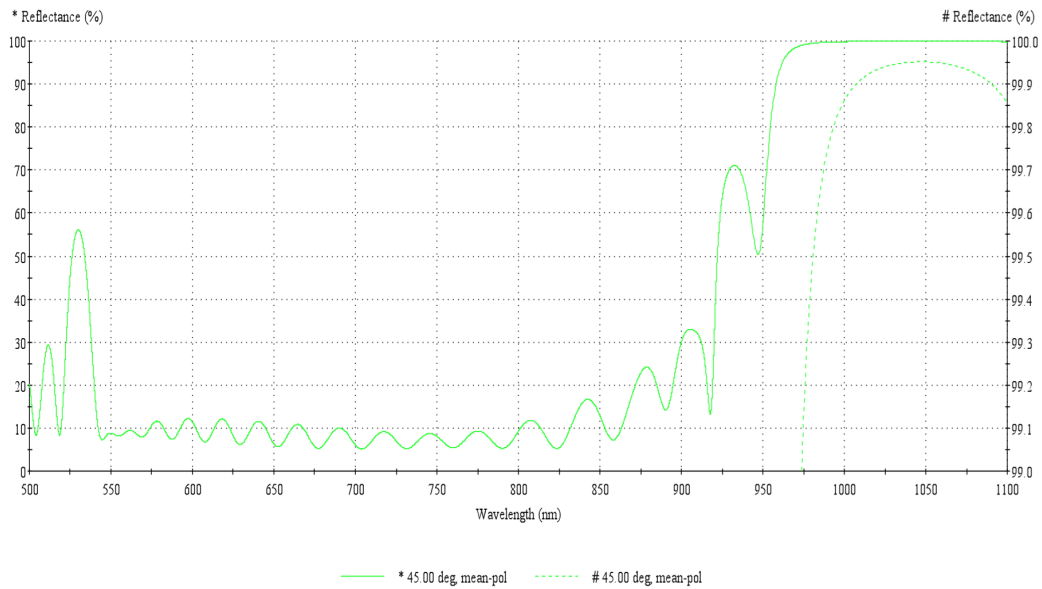


FIGURE 3.10: The simulated HR coating on the fused silica mirror for 45 degree of incident angle [22].

TABLE 3.6: Specification of Mirrors.

Mirror number	part number	Diameter [mm]	Incident angle	Polarization
MTx1	Y1S-1025-45 (CVI)	25.4	45	S
MTx2	Y1S-1025-45 (CVI)	25.4	45	S
MTx3	Y1S-1025-45 (CVI)	25.4	45	S
MTx4	Y1S-1025-45 (CVI)	25.4	45	S
MTx5	Y1S-1025-45 (CVI)	25.4	45	S
MTx6	Y1S-1025-45 (CVI)	25.4	55	S
MTx7	Y1S-1025-45 (CVI)	25.4	35	S
MTx8	Y1S-1025-45 (CVI)	25.4	45	S
MTx9	Y1S-1025-45 (CVI)	25.4	45	S
MTx10	Sigma-koki(TBC)	50.8	45	S
MTxU11	Sigma-koki(TBC)	50.8	45	S
MTxL11	Sigma-koki(TBC)	50.8	45	S
MTxU12	Sigma-koki(TBC)	50.8	20.9	S
MTxL12	Sigma-koki(TBC)	50.8	24.1	S

TABLE 3.7: Specification of beam splitter [19].

Characteristic	Typical value	Unit	Note
Beamsplitter Type	Laser Line Plate Beamsplitters		
Beamsplitter Shape	Round		
Wavelength Range	800	nm	
Bevel/Chamfer	0.35 mm × 45 Degree		
Wedge Angle Tolerance	5	arcmin	
Coating Material	Laser Line Dielectric		
Angle of Incidence	45	Degree	
Clear Aperture	85	%	
Substrate/Material	Fused Silica		
Surface Flatness	$\lambda/10$		
Surface Quality	10-5	scratch-dig	
Beamsplitter Diameter	50.8	mm	
Beamsplitter Thickness	6.35 mm		
Thickness Tolerance	±0.25 mm		

angle (see Fig. 3.4). The pico-motor is made by New port [23], whose part number is 8822.

3.3.8 Beam splitter

To reduce the elastic deformation, we separate the beam with the beam splitter made by CVI laser optics for pushing the node points of mirror. The part number of beam splitter is BS1-1064-50-2025-45P. The diameter of the beam splitter is 2 inch. Table 3.7 shows the separation ratio of beam splitter.

3.3.9 Optical follower servo

In order to achieve the low-noise and accurate modulation, an active controller (servo) can modulate the waveform by means of feedback control. This feedback loop used for the Pcal is called as the Optical Follower Servo (OFS). The OFS will be used in the KAGRA Pcal as a means to reduce the relative power noise (RPN) of the laser. We will achieve maximum sideband to carrier suppression of the modulated output waveform. The block diagram of the OFS is shown in Fig. 3.11. The transfer function of this diagram can be described as

$$\frac{AG_1}{1 + AKSG_1G_2}, \quad (3.3)$$

where A is actuation factor, S is sensing factor, K is percentage of light power sampled, G_1 and G_2 are gain of feedforward and feedback.

We monitor the difference between test input and {out1,out2,out3} . For monitoring the performance of OFS, we read the location of monitor point. When we inject the signal, such as swept sine, gauss sine and hardware injection signal, we use input port. The estimation of the expected gain parameter is listed in Table. 3.8.

The KS corresponds to the trans impedance gain of detector. The detail of photo detector is described in Sec.3.3.10. According to Table. 3.8, we regard G_2KS as unity.

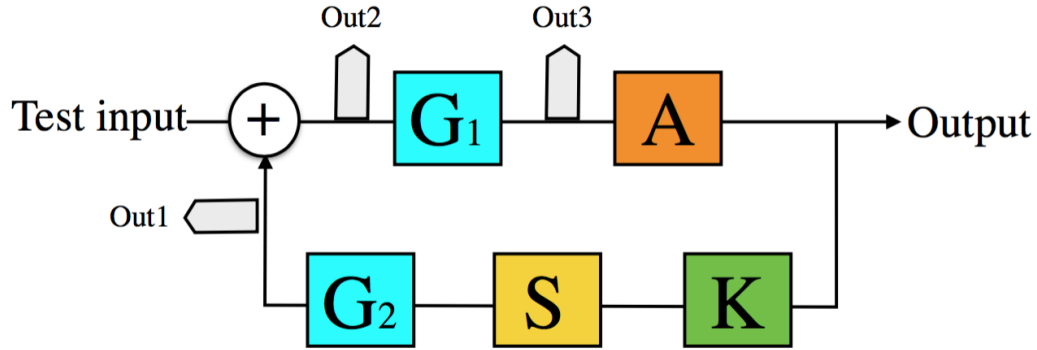


FIGURE 3.11: Diagram of feedback loop for OFS.

TABLE 3.8: Typical gain parameter of OFS.

	Gain	unit
A	0.5	W/V
G_1	10-100	V/V(dB)
G_2	2	V/V(dB)
KS	0.5	V/W

Therefore, we can simplify the transfer function as follows:

$$\frac{AG_1}{1 + AG_1} \quad (3.4)$$

We require the band width of OFS much larger than operation frequency. We employ the AOM as modulator, which made by ISOMET [24]. The part number of AOM is M1080-T80L-M. The specification is shown in Table 3.9

3.3.10 Photo detector

To detect the laser power, we use the photo detector. We place the photodetector at the working standard, Optical follower servo, Integrating sphere in Tx and Rx module. We developed the photo detector as shown in Fig. 3.12. We employ the InGaAs photo diode for absolute power measurement. The InGaAs diode is placed on the circuit board. The beam is collimated for the power detection reasonably.

Cover

The cover is designed by the LIGO Pcal group. We make the detector cover in Academia Sinica, Institute of Physics. Figure 3.13 shows the machined detector covers. We housed the circuit board into the cover coated by the black anodized aluminum (MIL-A-8625F, TYPEII,CLASS2).

InGaAs detector

We employ the C30665GH, which is large area InGaAs PIN photodiode with diameter of 3.0 mm with a flat glass window. The C30665GH provides high quantum

TABLE 3.9: Specification of AOM [24].

Characteristic	Typical value	Unit	Note
Spectral Range	0.36 > 1.5	μm	
AR Wavelengths	700 -900 or 1064	nm	
Interaction Medium	Tellurium Dioxide (TeO ₂)		
Acoustic Velocity	4.2	m/ μs	
Centre Frequency (Fc)	80	MHz	
RF Bandwidth	30	MHz	
Input Impedance	50	Ω	
VSWR	<1.5:1 @ Fc		
Clear Aperture	3.5	mm	
Active aperture	1.5	mm	
Static Insertion Loss Reflectivity	<3	%	
Laser Polarization	Any		
DC Contrast Ratio	1000:1 min		
Cooling	conduction		
Optical Power	20	W	
Beam Diameter	0.5	mm	
Optical Rise Time	77	ns	
Deflection efficiency	>85	%	Pol.: Perpendicular to Base
RF power	2.8	W	1064nm
Bragg angle	10.5	mrad	1064nm

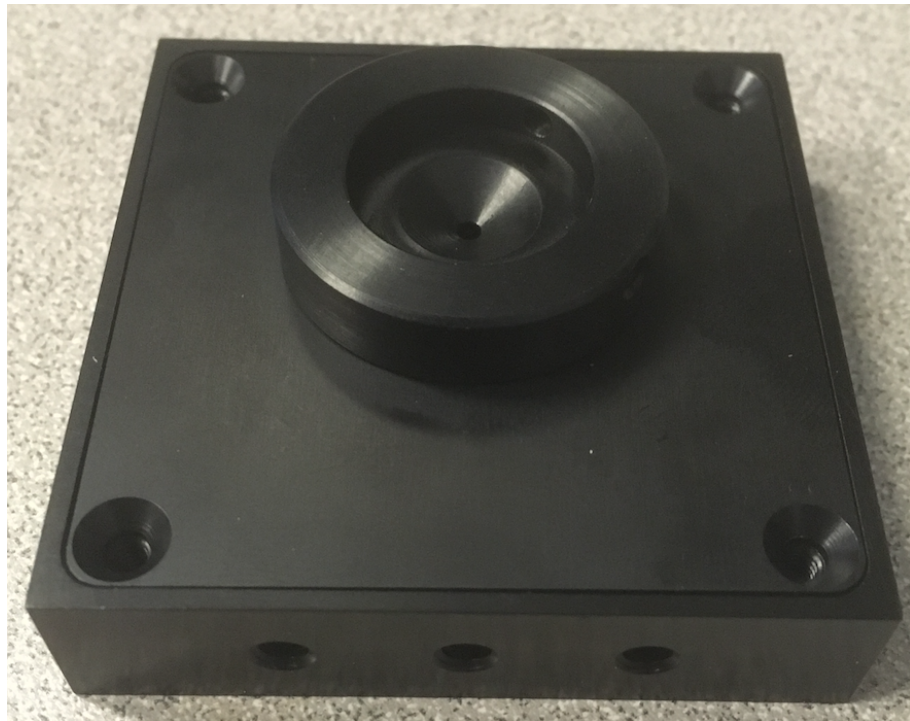


FIGURE 3.12: Developed photo detector for KAGRA Pcal.

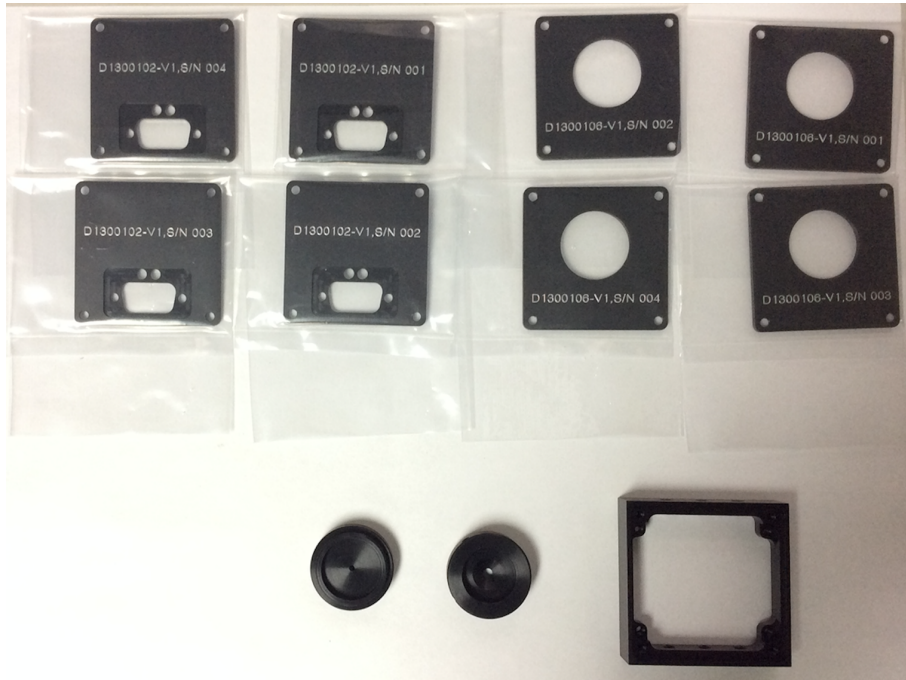


FIGURE 3.13: Fabricated cover.

TABLE 3.10: Specification of InGaAs detector.

Characteristic	Typical value	Unit	Note
Dark Current	25	nA	
Peak Wavelength	1550	nm	
Responsivity	0.95	A/W	
Breakdown Voltage	50	V	
Capacitance	200	pF	

efficiency from 800 nm to 1700 nm. This detector is fabricated by Excelitas [25]. The specification of detector is shown in Table. 3.14.

Electrical Circuit

We newly improved the electrical circuit of the photon detector as shown in Fig. 3.14. The electrical circuit is housed in the aluminum cover. We place the photo detector at the the behind of the electrical circuit. The layers of the circuit consists of 4 layer. We change the differential gain by changing the register and capacitor of the circuit. The electrical circuit are shown in Fig. 3.15.

3.3.11 Beam sampler

To make the feed back loop, we need to pick up the laser output using the beam sampler. LIGO uses the polarization beam sampler, which is significantly sensitive to incidence polarization angle. To avoid this difficulty, we plan to employ the diffractive beam sampler. Diffractive beam sampler is used to monitor high power lasers where optical losses and wavefront distortions of the transmitted beam need



FIGURE 3.14: The picture of photo detector. The diameter of photo detector is 3 mm. We control the incident power by changing diameter of the collimator and resistance of trans impedance amplifier

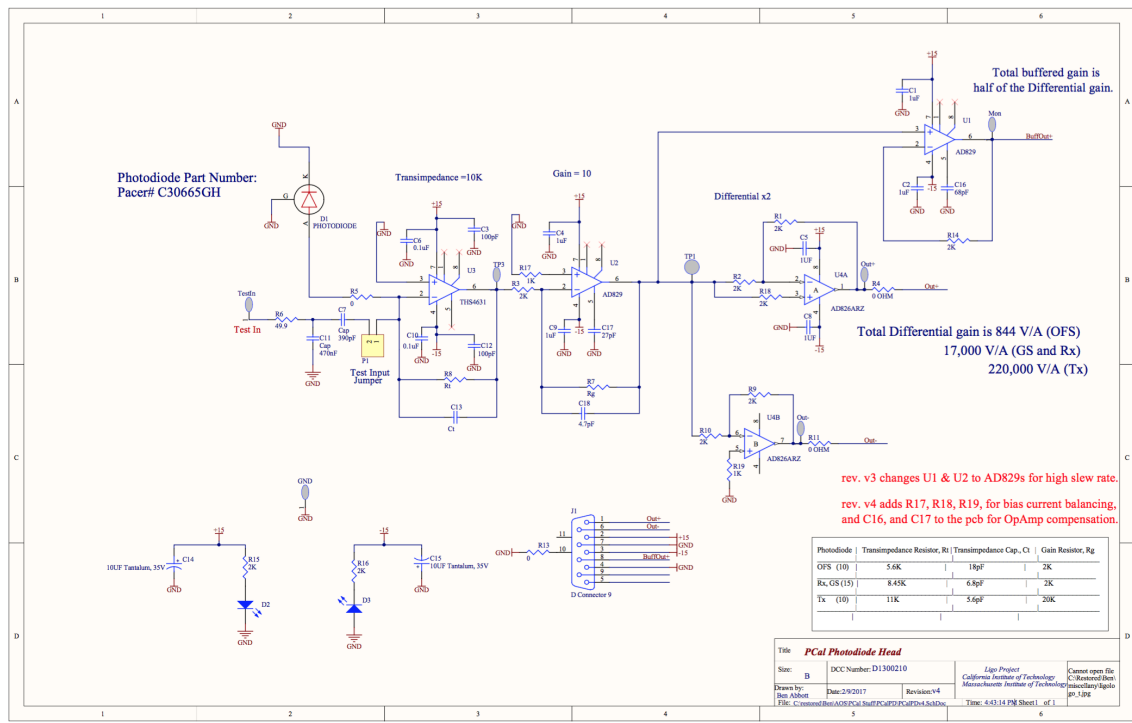


FIGURE 3.15: Circuit of photo detector designed by LIGO (D1300210-v4).

to be kept to a minimum. In most applications, most of the incident light must continue forward, "unaffected," in the "zero order" while a small amount of the beam is diffracted into a higher order, providing a "sample" of the beam. We will use the SA-220-1047-Y-A made by HOLO/OR Ltd [1].

The operational principle is quite straightforward. From a collimated input beam, the output beams exit from Diffractive Optical Element (DOE) with a separation angle that is determined during the design of the DOE. The beams separation is designed for far-field so that as the beams continue to propagate after DOE. A Diffractive Beam Sampler allows the high power beam (zero order) to propagate along the optical axis, but produces two side beams with low energy. These two sample beams are located to the left and right of the main beam (-1 and +1 orders).

3.3.12 2 inch integrating sphere

The 2 inches integrating sphere is used for the absolute power measurement of the laser. We receive the separated laser beam at beam sampler. We mount the photo detector (TxPD) at the port of integrating sphere. The integrating sphere is made by the Lab sphere. The inner surface of the integrating sphere is mounted on the Spectralon [26]. The measurement of the absolute power is described in Chap. 5

3.3.13 Structure

The breadboard is placed on the support structure. The material of this structure is SUS 306. This structure can be housed electrical devices, such as driver of the fiber laser, electronics of optical follower servo, and driver of laser shutter.

3.4 Periscope

The periscope is used for sending the beams to the ETM. We place the periscopes in EXA/EYA chamber as shown in Fig. 3.16. They consist of four periscopes. The first periscope is mounted at the vacuum side of the window. The laser is sent to second periscope on optical table. We share one first mirror and one second mirror for the two beams of the laser. We send the two laser to two third periscope. The third periscope is sent to fourth periscope, which is aligned to same height of the injected beam to the ETM.

3.4.1 Geometric optics

We consider the beam separation and focus position of the beams through the optical component. We fixed 80 mm separation of the mirror in transmitter module. Figure 3.17 shows the schematic view of optical layout, where D_{win} , D_{m2} , and D_{m3} are separation of beams, L_{win} , L_{m2} , and L_{m3} are distance of each components. We calculated the beam separation of the vacuum window, second mirror, and third mirrors by changing the focus point as shown in Fig. 3.18. X axis shows the distance from the window. We find a optimal point of minimum separation of the window because of clear aperture of window and second mirror. The optimal focus point is at 355 mm from the window corresponding to 108 mm separation of the mirror. We also find a incident angle of window with optimal focus point as 1.6 degree.

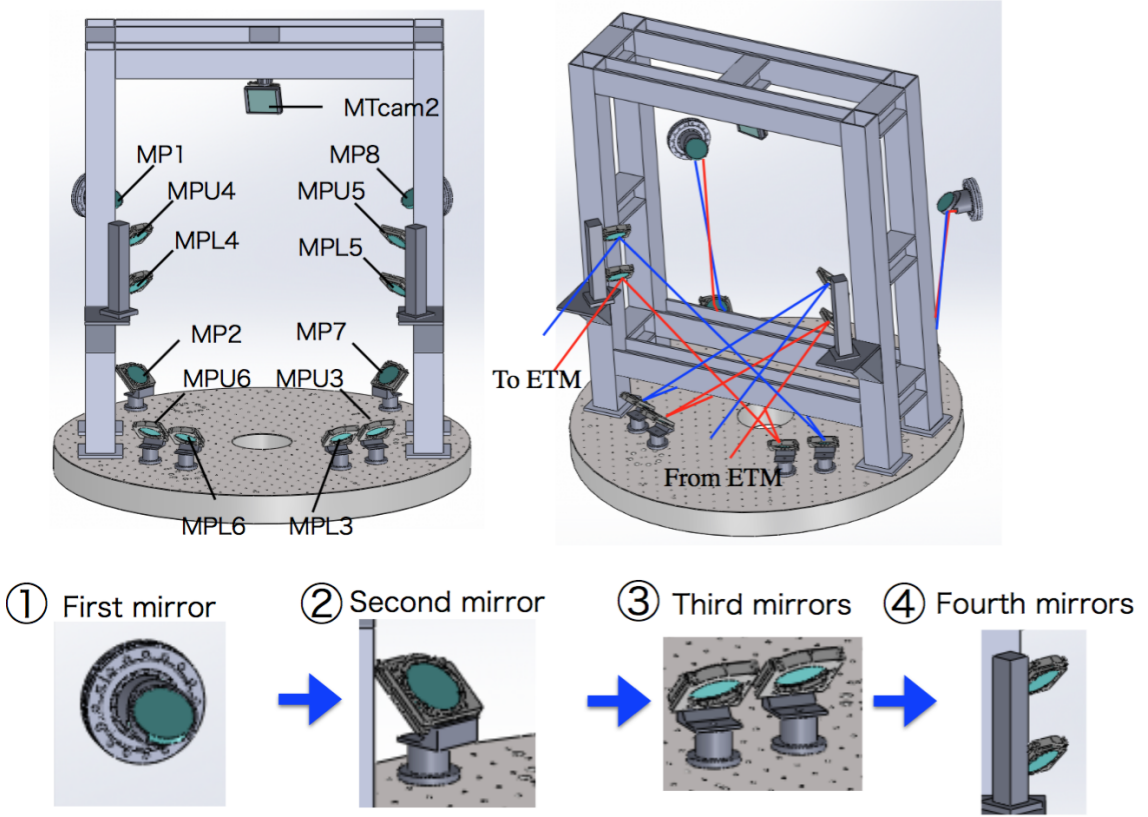


FIGURE 3.16: Periscope structure. We place the twelve 3-inch mirrors in total. The red and blue line correspond to lower and upper beam path, respectively. The upper and lower beams push the node point of the mirror surface.

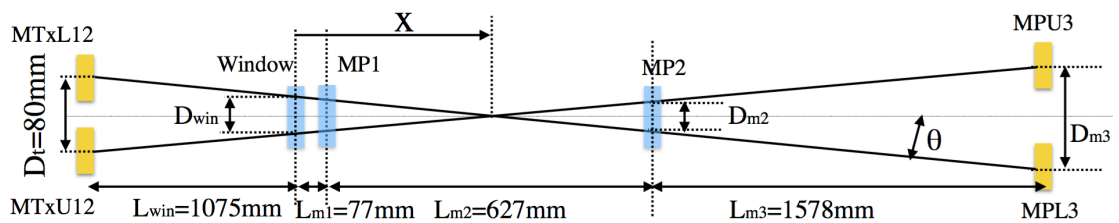


FIGURE 3.17: Schematic view of periscope position. We optimized the periscope positions. We fix the separation of Tx module mirror, and each distance, L_{win} , L_{m1} , L_{m2} and L_{m3} . x is distance from the window.

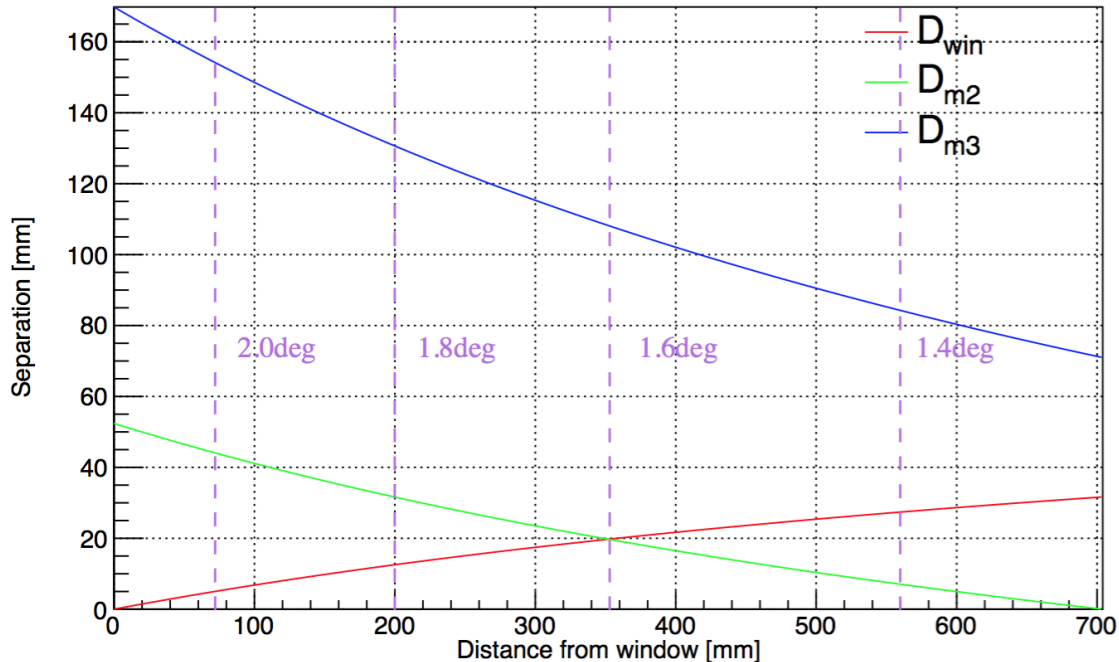


FIGURE 3.18: Calculated separation of D_{win} , D_{m2} , and D_{m3} by changing the distance from the window. Blue, Green and Red curves are separation position on the window, MP2 and MP3. Purple dashed lines are incident angle of the laser to window. We find the optimal point at 355 mm point corresponding to 1.6 degree incident angle.

TABLE 3.11: Simulation parameter for ANSYS [28]

Name	Fused Silica	SUS306
Young's module	73 Gpa	193 Gpa
Poison ratio	0.17	0.31
Density	2.201g/cm ³	7.750g/cm ³

3.4.2 View port window

One of the serious systematic errors are optical efficiency of the view port. Therefore, we have to reduce the reflectance of view port at least 0.1 % below. We employ the fused silica optical window whose diameter and thickness are 100 mm and 0.5 inch. We place the AR coating on both surfaces of the window. Figure 3.19 shows the simulated transmittance of the view port. The clear aperture of the view port is about 3 inch. The incident angle of the beams are 1.6 degree. We mounted the first periscope at the vacuum side of the window because we should avoid optical lever path. We set the incident angle of the periscope mirror as 50 degrees.

The flange type of the view port is ICF152. We remodeled the blank flange of ICF 152 made by Cosmotech [27]. Figure 3.20 shows the drawing of the view port. We employ the G-85 o-ring for vacuum sealing. We have simulated the deformation of window using ANSYS [28]. The assumed Young's module, Poisson ratio and density are listed in Table 3.11. The deformation of the window center is 0.85 μ m.

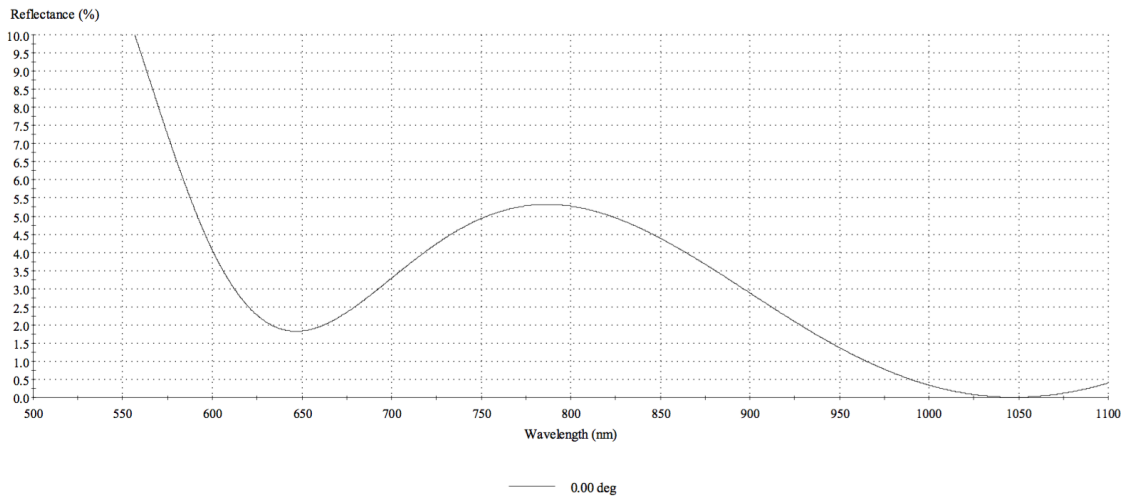


FIGURE 3.19: Simulated reflection of AR coating of one surface. We optimize the coating frequency at 1047 nm. This plot is provided by Sigma-koki.

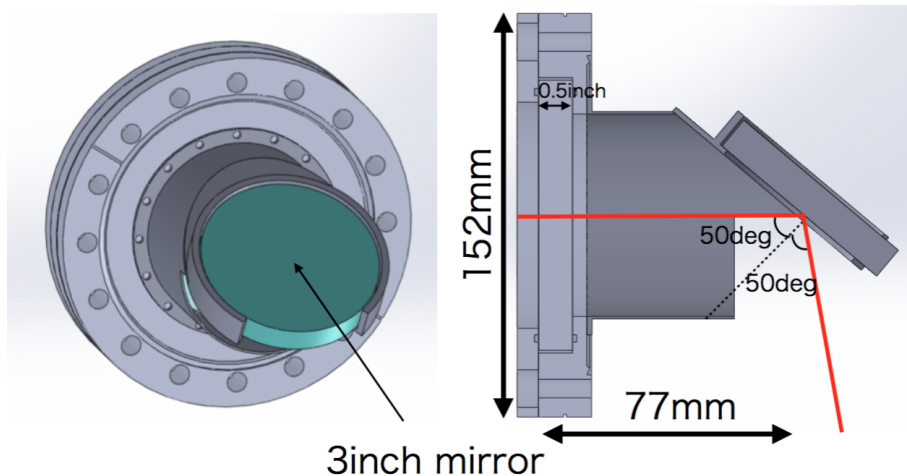


FIGURE 3.20: View window with periscope. We mount the AR coated fused silica window on the ICF152 flange. The AR coating is optimized at 1047 nm. We mount the periscope at the vacuum side of the window. The incident angle of the periscope is 50 degrees.

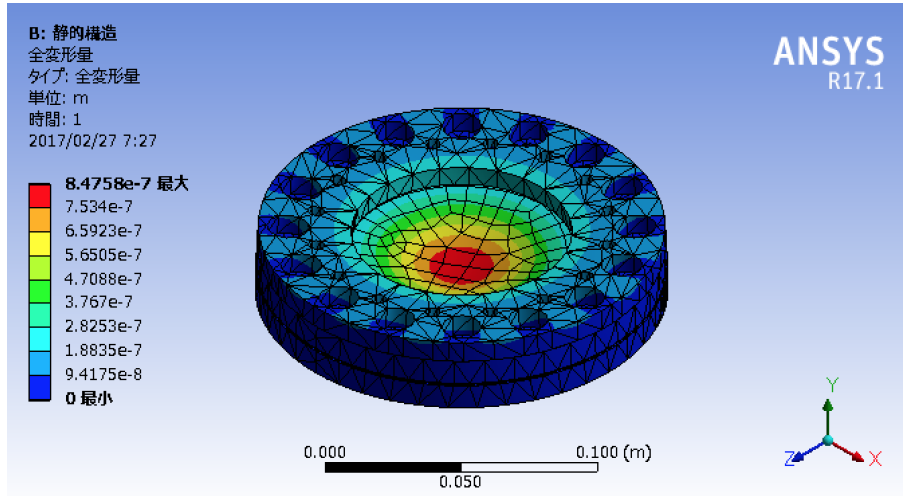


FIGURE 3.21: Simulated deformation of Pcal window [28]. The center deformation is $0.85 \mu\text{m}$.

TABLE 3.12: Specification of Mirrors in periscope.

Mirror number	part number	Diameter [mm]	Incident angle	Polarization
MP1	Sigma-koki(TBC)	76.2	50.0deg	P
MP2	Sigma-koki(TBC)	76.2	50.0deg	P
MPU3	Sigma-koki(TBC)	76.2	26.3deg(TBD)	(TBD)
MPL3	Sigma-koki(TBC)	76.2	26.5deg(TBD)	(TBD)
MPU4	Sigma-koki (TBC)	76.2	42.9deg(TBD)	(TBD)
MPL4	Sigma-koki(TBC)	76.2	41.7deg(TBD)	(TBD)
MPU5	Sigma-koki (TBC)	76.2	26.5deg(TBD)	(TBD)
MPL5	Sigma-koki (TBC)	76.2	26.3deg(TBD)	(TBD)
MPU6	Sigma-koki(TBC)	76.2	41.7deg(TBD)	(TBD)
MPL6	Sigma-koki (TBC)	76.2	42.9deg(TBD)	(TBD)
MP7	Sigma-koki (TBC)	76.2	50.0deg	P
MP8	Sigma-koki (TBC)	76.2	50.0deg	P

3.4.3 Mirrors

We employ eight 3 inch mirrors. We place the HR coating on the polished fused silica disc. The coating and polishing the fused silica is made by Sigma-koki corporation [22]. The reflectance of the mirror is shown in Fig. 3.10 and 3.9. The reflectance of HR coating depends on the incident angle and the polarization angle. The specification of mirrors are summarized in Table. 3.12.

3.5 Receiver module

The purpose of the receiver module is to measure the absolute power of laser and beam position control. All the components are mounted on the optical bench 300×600 mm optical table (B6030L, Tourlabs) [16]. The optical bench is mounted on the structure. To accomplish the purpose, we introduce QPD and 6 inch integrating

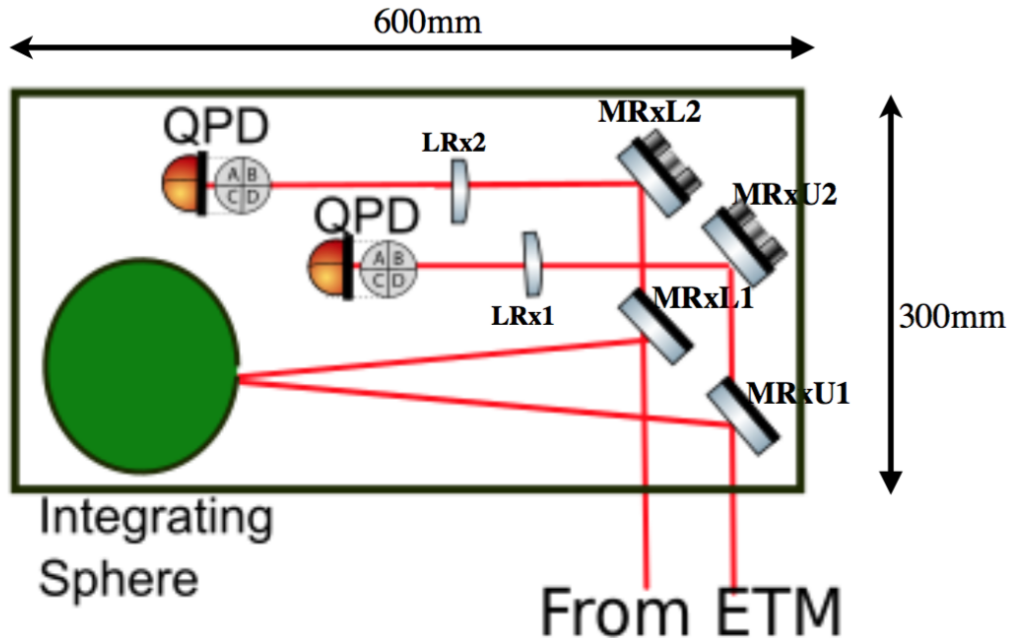


FIGURE 3.22: Optical layout of receiver module. We mounted QPD for monitoring beam position drift. Total power of the laser is measured by the integrating sphere.

TABLE 3.13: Specification of Mirrors in Rx module.

Mirror number	part number	Diameter [mm]	Incident angle	Polarization
MRxU1	Sigma-koki	76.2	47deg	S
MRxL1	Sigma-koki	76.2	43deg	S
MRxU2	Sigma-koki	76.2	45deg	S
MRxL2	Sigma-koki	76.2	45deg	S

sphere. The accuracy of beam position and absolute power are corresponding to the systematic errors.

3.5.1 6 inch Integrating sphere

The 6 inches integrating sphere is used for absolute power measurement of the laser. We receive the laser beam from two paths. To receive the power perfectly, we need a large diameter hole of integrating sphere at least 2 inch. We use for the 2 inch hole integrating sphere. We mounted the photo detector at the top of port. Details of the photo detector is explained in Sec. 3.3.10.

3.5.2 Mirror

We employ four 3 inch mirrors. We place the HR coating made by Sigma-koki as shown in Fig. 3.10 and 3.9. For two mirrors, we make the AR coating on the back surface to pick up the beams. The specification of the mirrors are listed in Table 3.13.

TABLE 3.14: Specification of QPD.

Characteristic	Typical value	Unit	Note
Substrate	InGaAs		
Wavelength Range	1000 - 1700	nm	
Detector Bandwidth	150	kHz	
Recommended Spot diameter	ϕ 0.2 - 0.5	mm	

3.5.3 QPD

We will implement QPDs for beam position control, which made by Tholabs. They also help us to understand the alignment drifts of the beams. The part number of QPD is PDQ30C as shown in Table. 3.14.

3.6 Camera module

The beam position of the ETM surface corresponds to systematic error of the rotation and elastic deformation. To measure the beam position, we measure the mirror surface directly. However, the KAGRA EXA/EYA chambers are placed at 36 m far from the ETM. Thus, we employ the combination of telescope and high resolution camera, we call telephoto camera (TCam). We are tuning with focus point of the mirror using focuser. We place the view port and mirror between the ETM and TCam. Figure 3.23 shows the drawing of TCam unit.

3.6.1 Camera

Purpose of using the high resolution camera, we have to measure the beam position within 1 mm accuracy. Ww solved this problem by D810 digital camera made by Nikon [29]. The D810 reprises the 36-megapixel resolution with 35.9×24.0 mm CMOS sensor. We remove the IR filter because the commercial camera is not sensitive to laser wavelength (1047 nm).

3.6.2 Telescope

We employ the Maksutov-Cassegrain type telescope for observing the ETM surface. The diameter of the primary mirror is 127 mm and its focal length is 1500 mm ($f/12$). The telescope is manufactured by Sky-watcher company [30]. The diameter of the telescope is limited by the that of the view window size.

3.6.3 Focuser

A focuser, which is made by Moonlight, is used for the automatic focus control. We connect focuser between telescope and camera. The picture of focuser is show in Fig. 3.24.

3.6.4 View port window

The flange type of the view port is ICF203. We remodeled the blank flange of ICF 203 made by Cosmotech [27]. Figure 3.25 shows the drawing of the view port. We employ the G-135 o-ring for vacuum sealing.

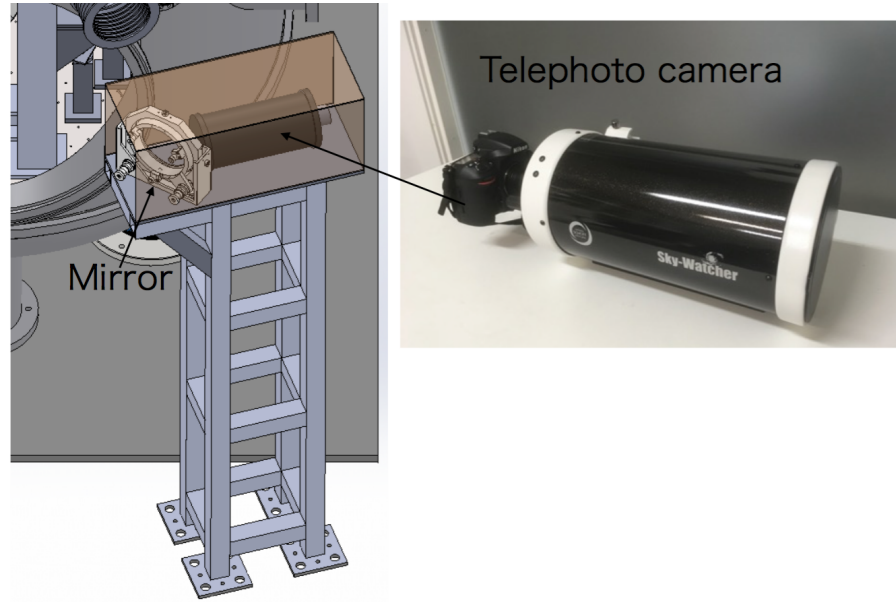


FIGURE 3.23: Mirror and Telephoto camera (TCam). We place the TCam on the structure. The image of ETM is referred by two mirrors. One mirror is mounted in vacuums. Another is placed at outside of chamber. The specification of mirrors are listed in Table. 3.15.



FIGURE 3.24: Moon light focuser.

TABLE 3.15: Specification of mirrors in camera

Mirror number	part number	Size [mm]	Incident angle
MTcam1	TFA-150C20-10 (Siguma-koki)	$\phi 150$	45deg
MTcam2	TFA-80100R15-10 (Sigma-koki)	100×80	30 deg

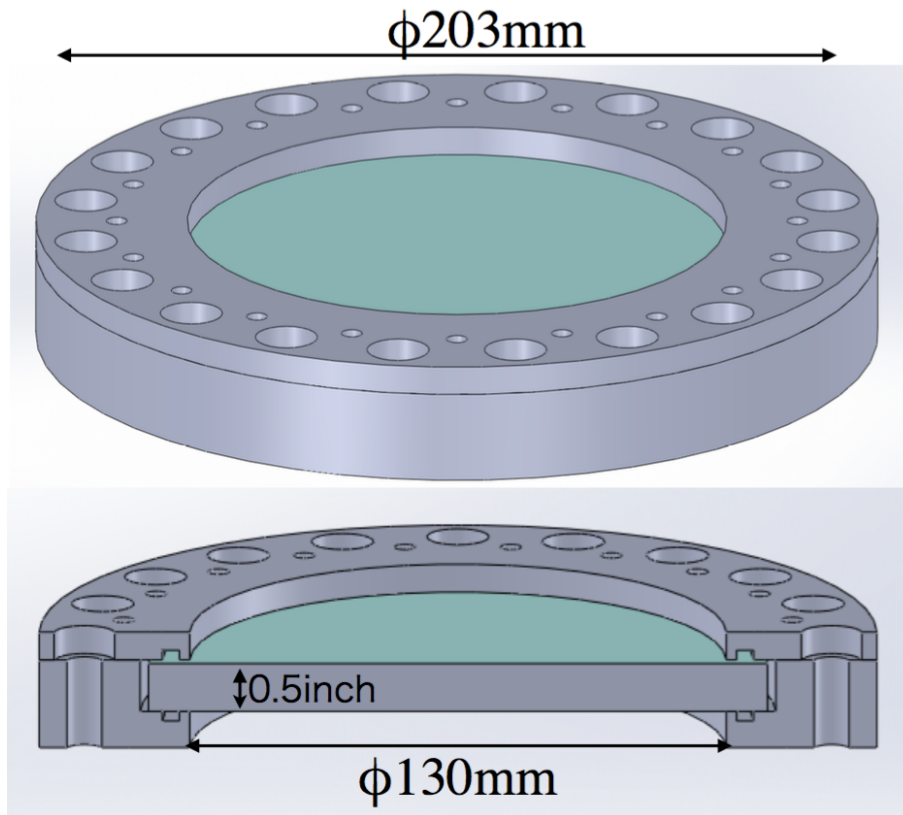


FIGURE 3.25: Window design. We employ the AR coated fused silica window.

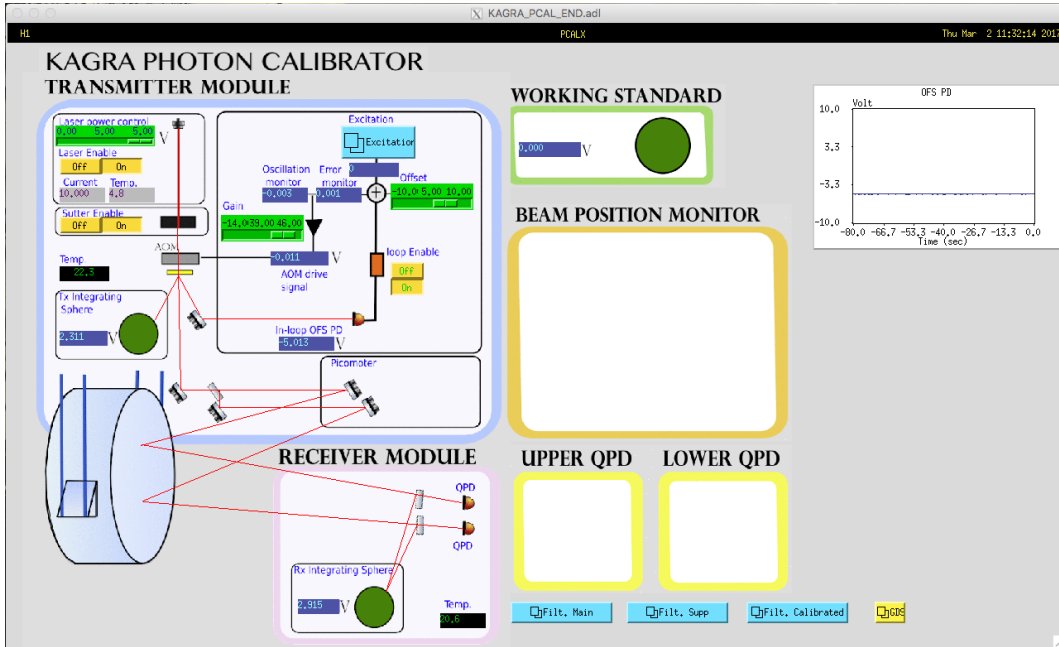


FIGURE 3.26: MEDM of KAGRA photon calibrator. The system is based on LIGO MEDM. We improve this system for BPM.

3.6.5 Mirror

We mount the two mirrors for Tcam. One mirror place in EXA/EYA chambers, whose size is 100×80 mm. This mirror is made by Thorlab. another mirror is mounted on the structure of the camera mount, whose diameter is 150 mm. The specification of the mirrors are listed in Table 3.15 .

3.6.6 Illuminator

To illuminate the mirror surface for taking picture, we place the illuminator

3.7 MEDM

All the system are controlled by Epics-MEDM [31]. MEDM is a Motif graphical user interface for designing and implementing control screens, called displays, that consist of a collection of graphical objects that display and/or change the values of EPICS process variables. The supported objects include buttons, meters, sliders, text displays/entries, and graphs. It has two modes of operation, EDIT and EXECUTE. Displays are created and edited in EDIT mode, and they are run in EXECUTE mode. Figure 3.26 shows the prototype MEDM system for KAGRA PCal.

3.8 Summary

There is a need for future demonstration to better under standing how accurate measurement. Im particular, we should test the improved performance of high power laser, and beam position monitoring system (BPM). Overall, our optimized instrumental design make the essential role of systematic error understanding for KAGRA

and other experiment. The strengths of one design are high power laser, symmetrical optical design, and BPM. These technology make the understand character of IFO easier. Finally, we show that this novel techniques is a promising tools to generate significant GW data.

Chapter 4

Elastic deformation

Calibration of interferometer above 1kHz is a challenging task. It was demonstrated that the calibration forces applied by a centered photon calibrator beam produce local elastic deformations which significantly alter the sensed displacement of the interferometer [10, 32]. Even stiff materials like fused silica or sapphire experience small deformation when photon calibrator forces are applied. The response to the excitation forces can be represented by the appropriate linear combination of normal modes. These effects, however, can be mitigated by applying at least two beams diametrically opposed and sufficiently displaced from the center of the test mass. This scheme was tested and implemented in LIGO and advanced LIGO photon calibrator [5, 33]. In this chapter, the investigations to identify the modes and their effect on the calibrator performance are discussed.

The modal analysis and simulation of the elastic deformation are made by using Finite Element Analysis (FEA) software package, ANSYS [28].

4.1 Perfect Cylinder model

As the first step, we made the analysis in the perfect cylinder cases. Table. 4.1 shows two sets of parameters similar to LIGO and KAGRA end test mass (ETM). It is known that two normal modes are most relevant in the calibration frequency ranges. The mode resonant frequencies are also shown in Table. 4.1. In the following analysis a cartesian coordinate system is defined such that $x - y$ plane is on the circular surface of the cylinder and z axis is along the cylinder height.

4.1.1 Modal displacement parameterization

The directional displacements in z component, Δz can be well approximated by a simple polynomial function. For the drumhead mode, the displacement, Δz_{DH} can be written as:

$$\Delta z_{DH} = p_0 + p_1 r^2 + p_2 r^4, \quad (4.1)$$

where $r = \sqrt{x^2 + y^2}$ and, p_0 , p_1 , p_2 are polynomial coefficients. Figure 4.1 shows the fitting of FEA results by eq. 4.1. From this fitting we can estimate the drumhead node position, r_{DH} as the position where the z displacement is equal to 0.

For the butterfly mode, the displacement, Δz_{BF} can be parameterized as:

$$\Delta z_{BF} = (p_1 r^2 + p_2 r^4) \cos(2\theta + \theta_0), \quad (4.2)$$

where $\theta = \arctan(y/x)$ and θ_0 is a phase offset. Usually, we take $\theta_0 = 0$ and $\theta_0 = \pi/4$ for the two butterfly modes. The node lines where $\Delta z_{BF} = 0$ lie at $\theta = \theta_0 \pm \pi/2$. Fig. 4.2 shows $\Delta z_{BF} = 0$ as a function of r and θ in the LIGO case. The KAGRA case show very similar behavior. The four node lines lie at $\theta = \pm 1/4\pi$ and $\pm 3/4\pi$.

TABLE 4.1: Simulation parameters and results for perfect cylinder studies.

Quantity	LIGO	KAGRA
Diameter [mm]	340	220
Thickness [mm]	200	150.2
Material	Silica	Sapphire
Density [kg m^{-3}]	2203	4000
Weight [kg]	40.003	22.838
Poisson ratio	0.1631	0.3
Young's modulus [GPa]	72.6	400
Drumhead [Hz]	8109	23798
Butterfly [Hz]	5969	16058
Drumhead node [mm]	109.0	65.3

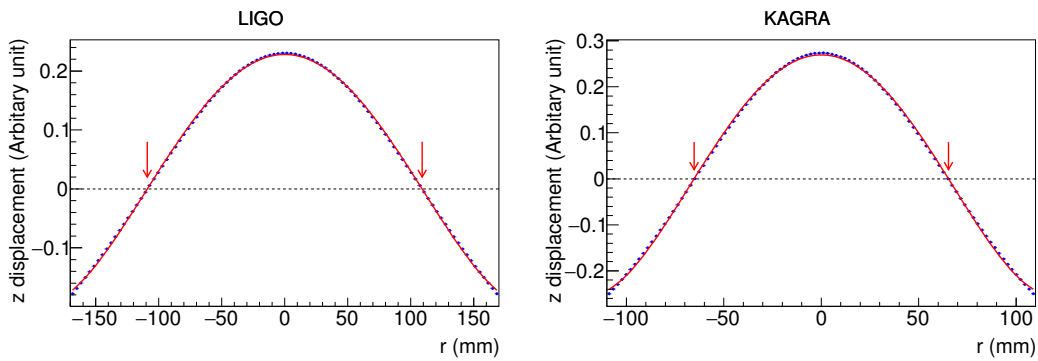


FIGURE 4.1: Fitting of z displacements, Δz_{DH} of the drumhead mode as a function of $r = \sqrt{x^2 + y^2}$ for LIGO case (left) and KAGRA case (right). The fitted node positions, r_{DH} , where $\Delta z_{DH} = 0$ are 109.0 mm and 65.3 mm for LIGO and KAGRA cases, respectively.

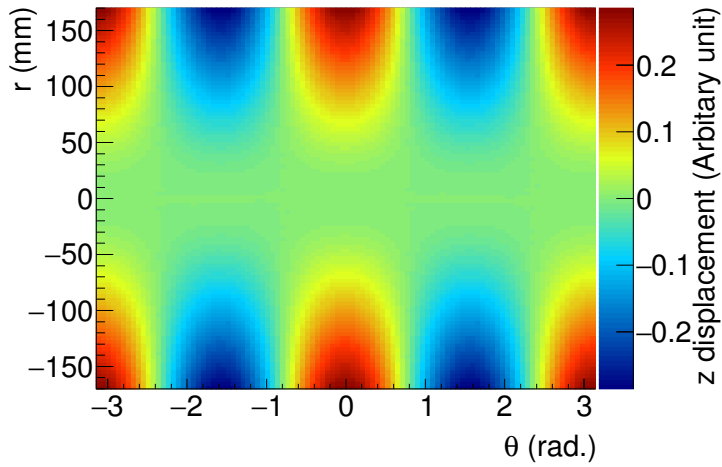


FIGURE 4.2: The z displacement, Δz_{BF} , for the butterfly mode as a function of $r = \sqrt{x^2 + y^2}$ and $\theta = \arctan(y/x)$ for the LIGO case. The KAGRA case show very similar behavior. The four node lines lie at $\theta = \pm 1/4\pi$ and $\pm 3/4\pi$.

4.1.2 Optimal beam position scan

The total displacement sensed by the main interferometer beam can be defined as the combination of the free-mass motion and the surface displacement due to the elastic deformation. The free-mass motion, D_{free} can be written as

$$D_{\text{free}}(f) = \frac{F}{m(2\pi f)^2}, \quad (4.3)$$

where F is an external force, m is the mirror mass and f is the frequency.

In the coordinate system that z -axis is along the main interferometer beam, the effective displacement sensed by the main interferometer beam, $D_{\text{eff}}(f)$ is represented by the surface integral on the HR plane, of the test mass, Ω_{HR} :

$$D_{\text{eff}}(f) = k_I \int_{\Omega_{\text{HR}}} D(x, y; f) I(x, y) dx dy, \quad (4.4)$$

where $D(x, y; f)$ is the total displacement at (x, y) for frequency f , $I(x, y)$ is the interferometer beam profile,

$$I(x, y) = \exp \left(-2 \frac{x^2 + y^2}{r_{\text{beam}}^2} \right), \quad (4.5)$$

and k_I is a normalization constant defined as:

$$k_I \int_{\Omega_{\text{HR}}} I(x, y) dx dy = 1. \quad (4.6)$$

In case of LIGO, $r_{\text{beam}} = 62$ mm and $k_I = 165.614 \text{ m}^{-2}$. In case of KAGRA, $r_{\text{beam}} = 35.3$ mm and $k_I = 2893.36 \text{ m}^{-2}$. Finally, the displacement ratio, $R(f)$ is defined as:

$$R(f) = \frac{D_{\text{eff}}(f)}{D_{\text{free}}(f)}. \quad (4.7)$$

TABLE 4.2: Simulation parameters and results for the KAGRA ETM CAD model.

Quantity	Cylinder	CAD model
Diameter [mm]	220	220
Thickness [mm]	150.2	150.2
Material	Sapphire	Sapphire
Density [kg m^{-3}]	4000	4000
Weight [kg]	22.838	22.994
Poisson ratio	0.3	0.3
Young's modulus [GPa]	400	400
Drumhead [Hz]	23798	23658
Butterfly [Hz]	16058	15913
Drumhead node [mm]	± 65.3	-66.5/62.7

Fig. 4.3 shows the displacement ratio, $R(f)$ as a function of frequency, f for optimally positioned beams and ± 2 mm and ± 4 mm offsets for LIGO case and KAGRA case. The cross check of the simulation is also done with COMSOL [34] and the agreement within 0.2 % has been obtained.

4.2 Real ETM model

The real structure of KAGRA ETM is not a perfect cylinder but has two flat cuts at both sides with two ears used to hang the mirror. Fig. 4.4 shows the CAD model of the KAGRA ETM. We made the similar FEA on the realistic KAGRA ETM structure. The results are shown in Table 4.2, which are very close to those obtained in the perfect cylinder model. Fig. shows the illustration of z displacements for two dominant modes, butterfly and drumhead modes. One particular effect in KAGRA ETM is that it is not symmetric in vertical direction along y -axis. Fig. 4.6

We made the same analysis as in Section 4.1.2 to obtain the optimal position of beams. Figure 4.7 shows the displacement between the sensed motion and free mass motion as a function of frequency for optimally positioned beams on KAGRA test mass, as well as ± 1 mm and ± 3 mm offsets from the optimal positions.

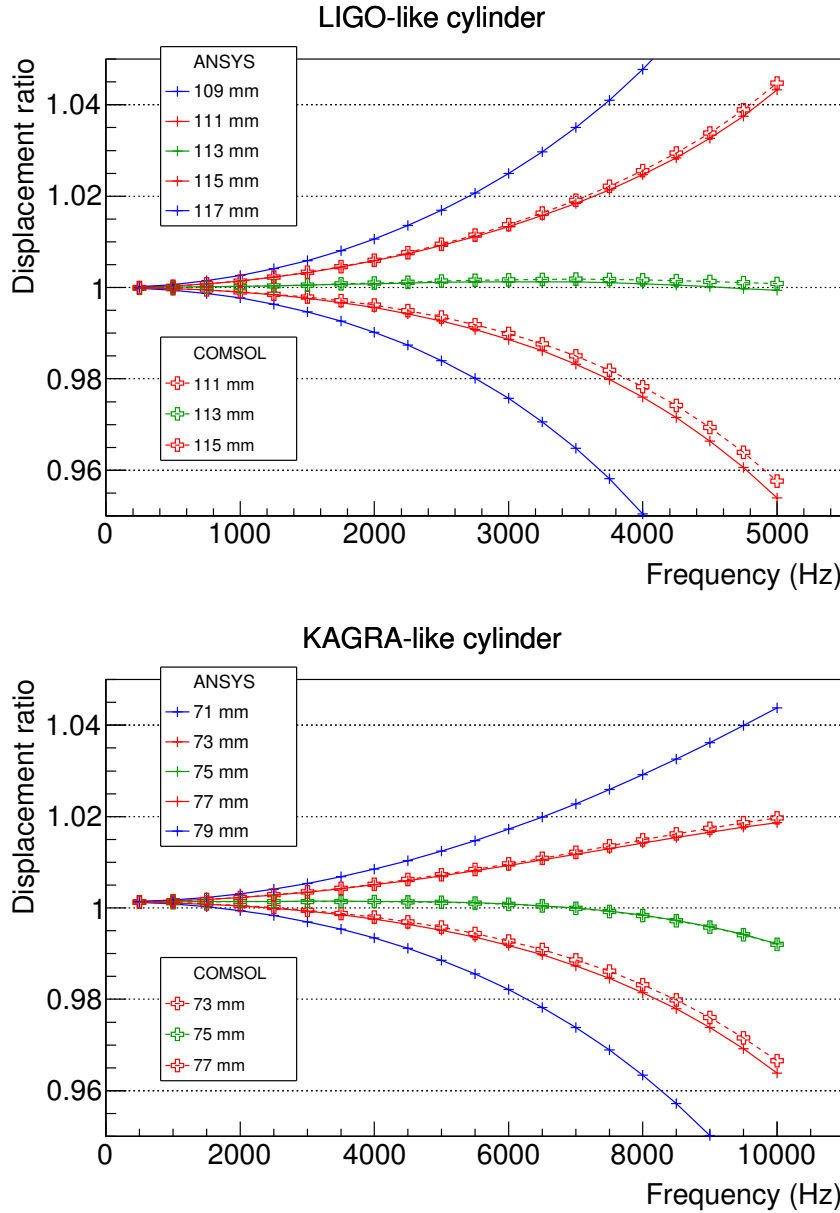


FIGURE 4.3: The ratio, $R(f)$ between the total sensed motion, $D_{\text{eff}(f)}$ and free mass motion, $D_{\text{free}}(f)$ as a function of frequency, f for optimally positioned beams and ± 2 mm and ± 4 mm offsets for (top) LIGO case and (bottom) KAGRA case. The cross check of the simulation is also done with COMSOL [34] and shown for optimum position and ± 2 mm offsets with open cross symbols.

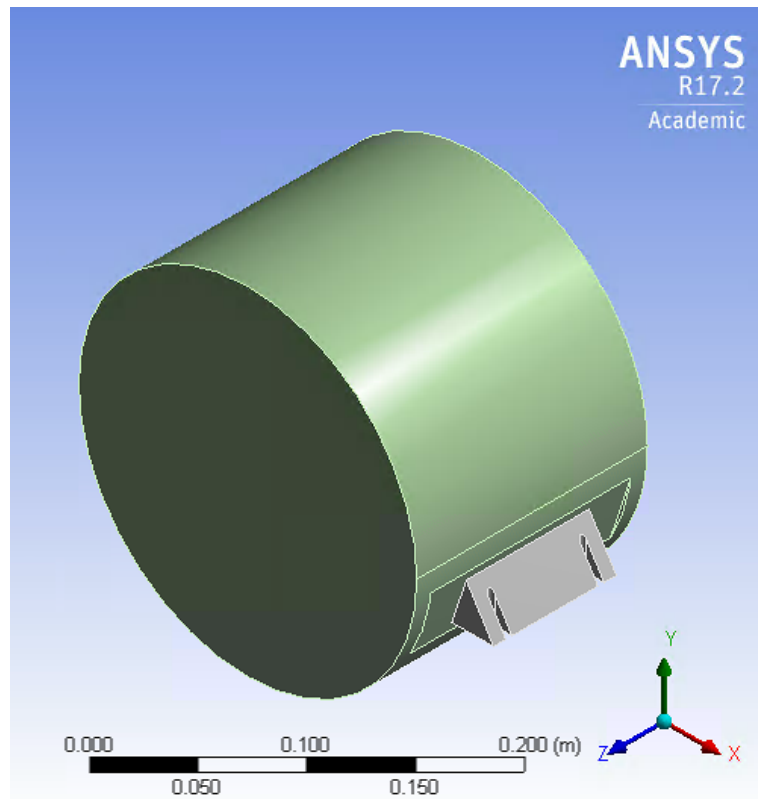


FIGURE 4.4: The CAD model of the KAGRA ETM with flat cuts and ears.

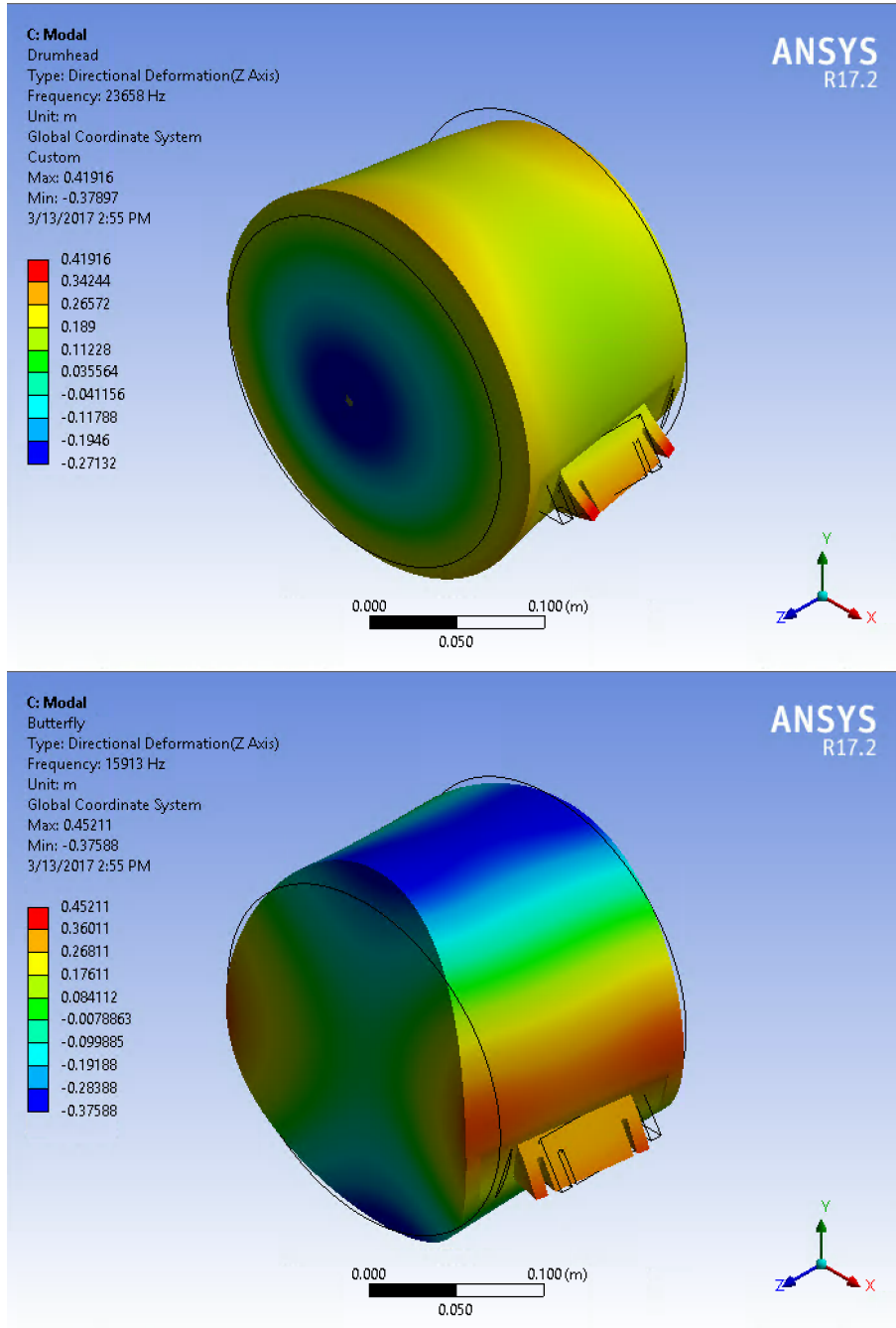


FIGURE 4.5: Drumhead (top) and Butterfly (bottom) modes for KA-GRA ETM.

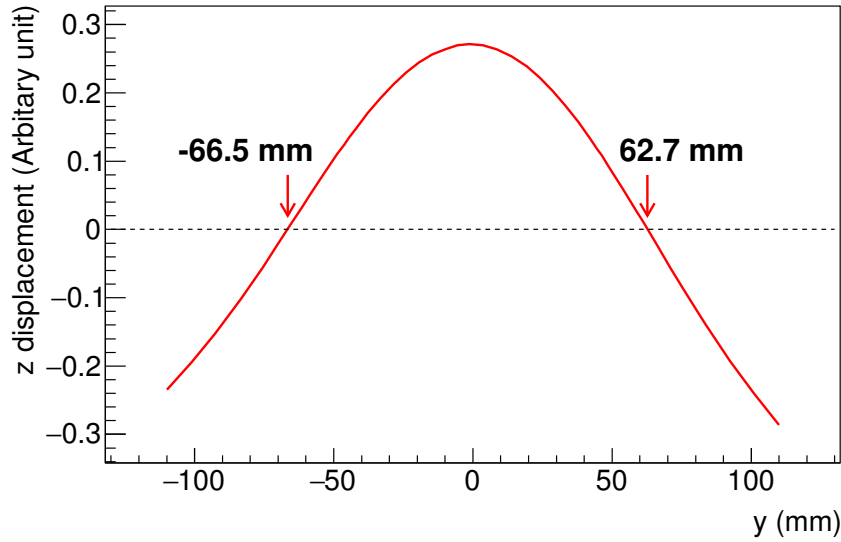


FIGURE 4.6: Fitting of z displacements, Δz_{DH} of the drumhead mode as a function of y for KAGRA ETM model. The fitted dnode positions, r_{DH} , where $\Delta z_{DH} = 0$ are asymmetric and located at -66.5 mm and 62.7 mm.

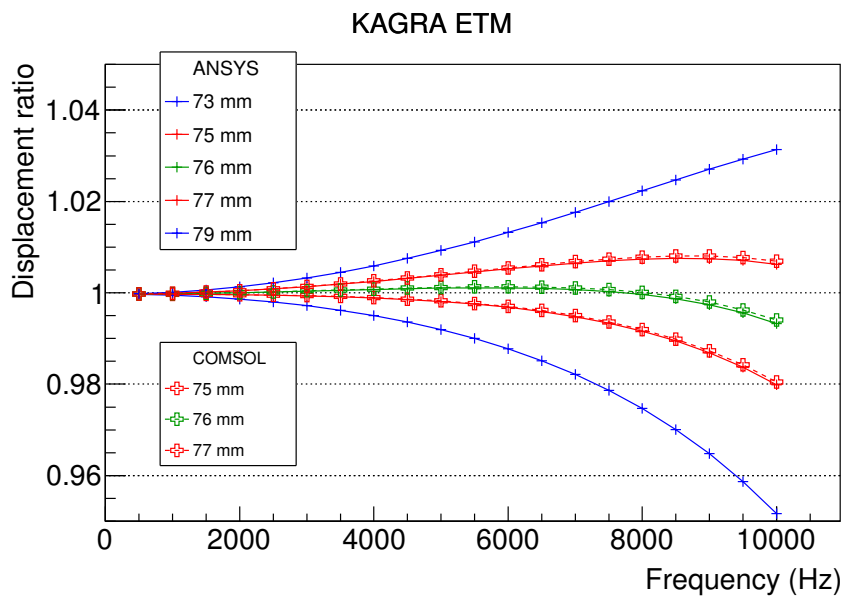


FIGURE 4.7: The ratio between the total sensed motion and rigid body motion as a function of frequency for optimally positioned baams and ± 1 mm and ± 3 mm offsets. The cross check of the simulation is also done with COMSOL [34] and shown for optimum position and ± 1 mm offsets with open cross symbols.

Chapter 5

Absolute power calibration

This chapter describes the absolute power calibration procedure of KAGRA photon calibrator. The systematic error of the absolute power is most largest in LIGO. They measure the laser power with integrating sphere and InGaAs photodetector because displacement of mirror corresponds to laser power. The absolute power injected to the ETM can be obtained as average of input power at Tx module and the output power at Rx module as follows:

$$P = \frac{P_{\text{TxPD}} + P_{\text{RxPD}}}{2} = \frac{1+e}{2e} P_{\text{RxPD}}, \quad (5.1)$$

where P_{TxPD} and P_{RxPD} are the measured power of the transmitter module photo detector(TxPD) and the receiver module photodetector (RxPD), and $e = P_{\text{TxPD}}/P_{\text{RxPD}}$ is optical efficiency. Therefore, P_{TxPD} and P_{RxPD} limit the calibration accuracy of the absolute displacement of the mirror. To calibrate P_{TxPD} and P_{RxPD} , we employ the working standard (WS) and the gold standard (GS).

The WS of KAGRA (WSK) is the combination of integrating sphere and InGaAs photo detector (see Fig. 5.1), which is calibrated against GS of LIGO (GSL) in LHO lab as calibrated by NIST. LIGO also make working standards for LHO and LLO as shown in Fig 5.2. The ratio of measured voltage of WS and GS detectors are obtained as

$$\frac{V_{\text{WSK}}}{V_{\text{GSL}}}. \quad (5.2)$$

We can calibrate the response of WS using GS through this equation.

We will also use the WSK to calibrate the TxPD and RxPD, which are inside the Tx module and Rx module of Pcal, respectively. We will measure the ratio of voltage of TxPD and RxPD as follows

$$\frac{V_{\text{TxPD}}}{V_{\text{KWS}}}. \quad (5.3)$$

Finally, we obtain the calibration power P_{GW} using the power standard laser in NIST. Then, we can get the calibrated P_{TxPD} and P_{RxPD} as follows:

$$P_{\text{TxPD}} = \frac{V_{\text{TxPD}}}{V_{\text{KWS}}} \frac{V_{\text{WSK}}}{V_{\text{GSL}}} P_{\text{GS}}, \quad (5.4)$$

$$P_{\text{RxPD}} = \frac{V_{\text{RxPD}}}{V_{\text{KWS}}} \frac{V_{\text{WSK}}}{V_{\text{GSL}}} P_{\text{GS}} \quad (5.5)$$



FIGURE 5.1: KAGRA working standard.

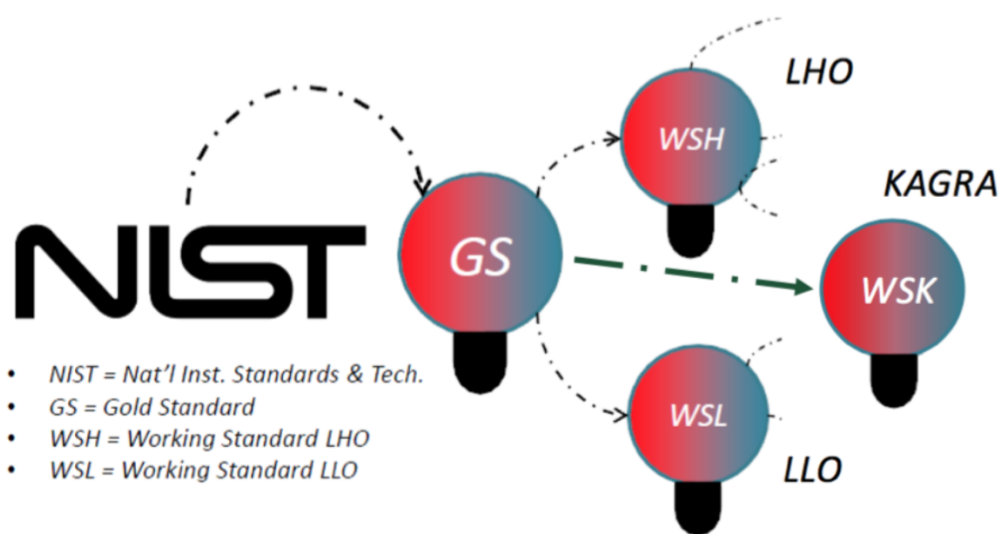


FIGURE 5.2: comparison with GS and WS.



FIGURE 5.3: Voltmeter made by keithlay.

5.1 Calibration in LHO

We explain the calibration of WSK in LIGO. To avoid systematic error of localization from GS, we need to calibrate the displacement of mirror by each interferometer. LIGO use the GSL calibrated by NIST for calibration of absolute power of LLO and LHO. We also calibrate WSK using same GSL. To accurate measurement, we bring the WSK, photo detector and voltmeter to LHO.

We employ the four inch integrating sphere made by Labsphere. The model number of the integrating sphere is 3P-LPM-040-SL. We mount the photo detector at the top of integrating sphere. The detail of photo detector is written at Sec. 3.3.10. The voltmeter is make by Keithley company as shown in Fig. reffig:Keithley. The model number of voltmeter is 2100/100. To reduce the instrumental bias, we fix the pair of voltmeter and WS.

We check the time trend of the optical efficiency, $V_{\text{GS}}/V_{\text{WS}}$ by 4 month.

5.2 Calibration in end-station

We calibrate the TxPD and RxPD in X/Y end station every month. When we calibrate the TxPD, we open the side box and mount the WSK as shown in Fig 5.4. We measure the power of two beams. We calculate the ratio between TxPD and sum of two beam voltage measured by WSK.

We also calibrate the RxPD. We replace from RxPD to WS and measure the ratio of the voltages.

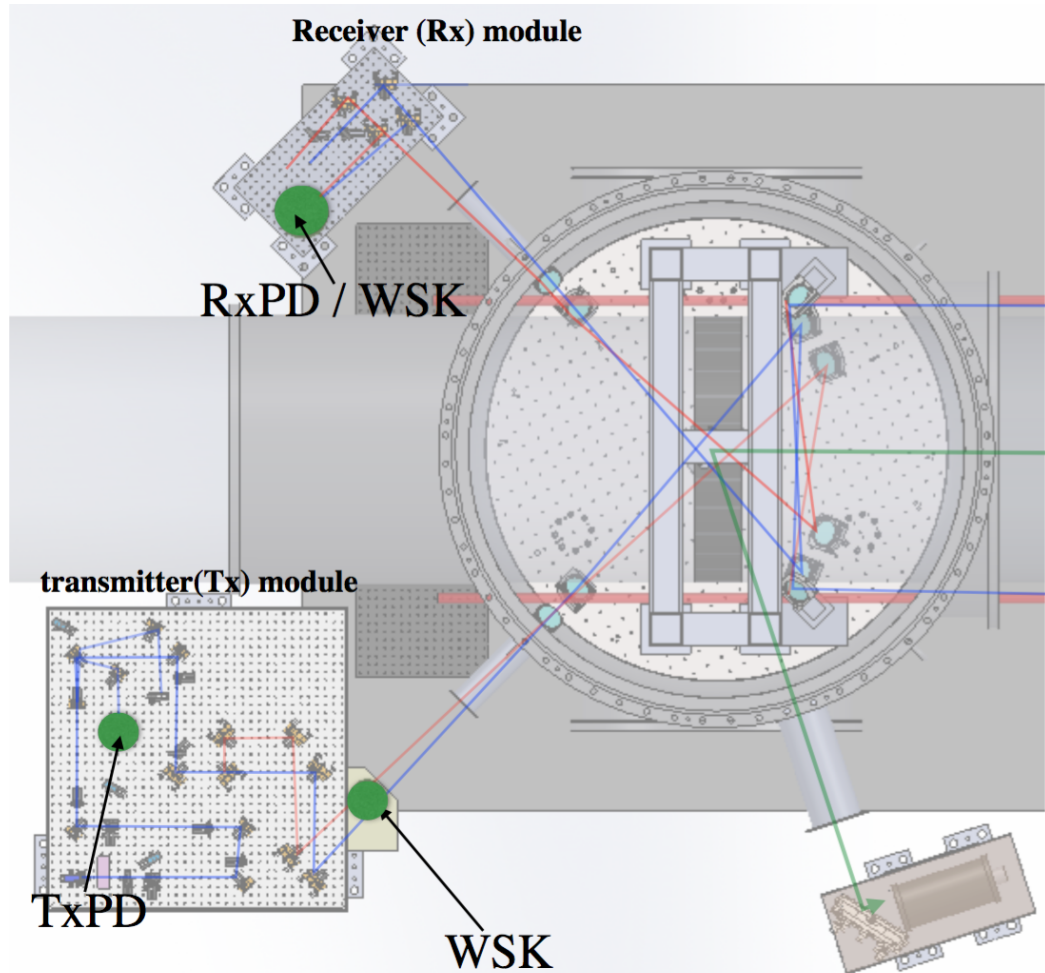


FIGURE 5.4: Calibration of end-station. We calibrate TxPD and RxPD using WSK.

We check the time trend of the optical efficiency, $V_{\text{TxPD}}/V_{\text{WS}}$, $V_{\text{RxPD}}/V_{\text{WS}}$, by 1 month.

Furthermore, we monitor the time trend of $V_{\text{TxPD}}/V_{\text{RxPD}}$, everyday.

If we find unstable region in time trend, we need to propagate the uncertainty as the systematic error.

5.3 Summary

This chapter has considered the absolute power calibration for KAGRA Pcal. The uncertainty of the displacement of ETM is corresponding to that of the absolute power of PCal laser. We will monitor the trend of each parameter because it propagate to the systematic error of $h(t)$.

Chapter 6

Beam position monitor

The serious systematic errors of the rotation and elastic deformation are from beam position. We are developing Beam Position Monitor (BPM) for accurate measurement of beam position. Previous study in LIGO have achieved 0.3 % of uncertainty of the beam rotation effect by using Telephoto camera system (TCam). They place the telephoto camera at 8 m far from the ETM. On the other hand, that of KAGRA is 36 m where is 4.5 times larger. Therefore, one of the most difficult technologies of calibration in KAGRA may be the beam position control. We will demonstrate the system of the BPM as the new technology. The BPM system is consists of QPD, Picometer, and TCam

According to Eq.(2.1), vector \vec{a} and \vec{b} corresponds to the rotation effect. \vec{a} can be written as

$$\vec{a} = \vec{a}_1 + \vec{a}_2, \quad (6.1)$$

where \vec{a}_1 and \vec{a}_2 are position vectors of two Pcal beams. We can measure the beam position of the main interferometer, \vec{b} , as well. We can obtain the rotation term as

$$\frac{I}{M} \vec{a} \cdot \vec{b}, \quad (6.2)$$

where I and M are the inertial moment and mass of test mass.

Furthermore, the misaligned beam positions make the elastic deformation on the mirror surface due to asymmetry injection. It is one of the serious systematic errors. Detail of the elastic deformation is described in Sec. 4.

6.1 Installation

The installation phase of beam position monitor consists of two phases. In first phase, we place the TCam system at the side of EXA and EYA chamber. Detail of TCam is described in Sec. 3.6. We connect the TCam and control PC (Raspberry pi) and operate it. The purpose of TCam is not only calibration work but also other application. We will monitor the pollution of water due to cryo-pumping effect. The taken picture will be analyzed automatically. In second phase, we place the QPD and the pico motor for monitoring the beam drift. We will control the beam position using these components.

6.2 Operation

All the system is operated by MEDM system as shown in Fig. 3.26. For monitoring the beam positions, we use two pictures, which are with and without illuminator. We use the is Open Source Computer Vision Librarly (OpenCV) in python for image

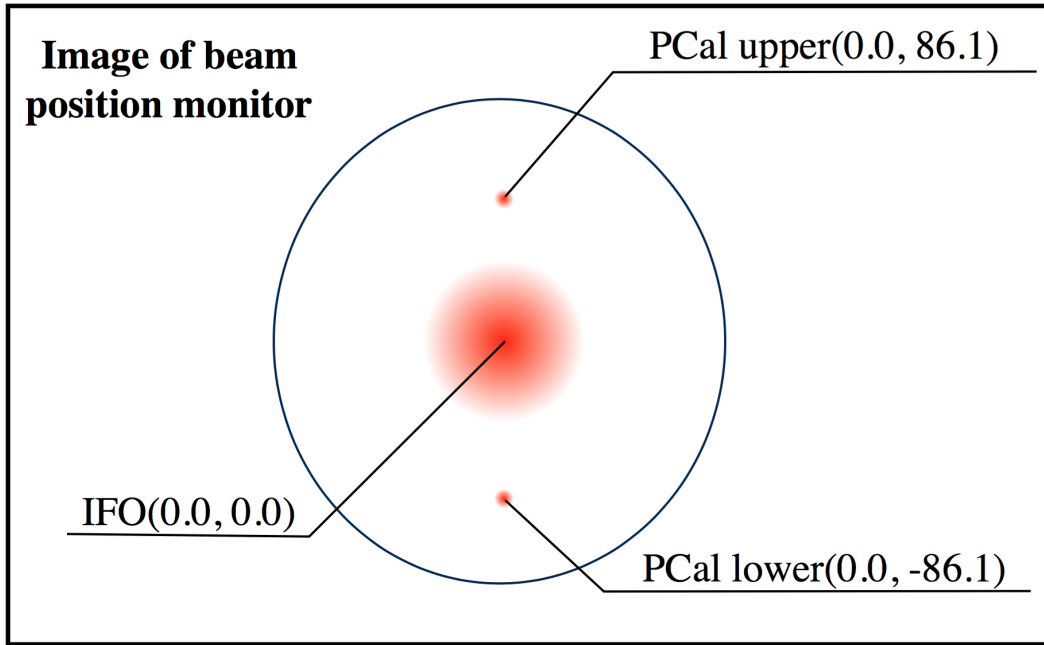


FIGURE 6.1: Image of beam position monitor. We will over-plot the estimated beam position on the picture.

analysis, which is a library for open source computer vision developed and released by Intel. The operation strategy is listed as follows:

1. Take a JPEG style picture with illuminator. We set the integration time to 30 sec.
2. Convert picture to gray scale using OpenCV.
3. Set the reasonable threshold to find a boundary of the edge of ETM.
4. Mask the analysis region to separate the ETM edge and others.
5. Estimate the origin of the mirror coordinate by fitting of edge shape of the mirror.
6. Turn off the illuminator and take picture with 30 sec integration time.
7. Estimate the Pcal beam position and main interferometer position with no illumination picture. Then, we fit the gray scale picture using Gauss function.
8. Make a picture overplotted the coordinate of Pcal and origin as shown in Fig. 6.1.

6.3 Demonstration test

We tried the demonstration test using TCam with 150mm diameter telescope and dummy target. Figure 6.2 shows the test setup.

We mount the target structure on the camera tripod. The size of target is 24 × 24 mm. Then, pixel size of this picture corresponds to 193 × 193. We can estimate

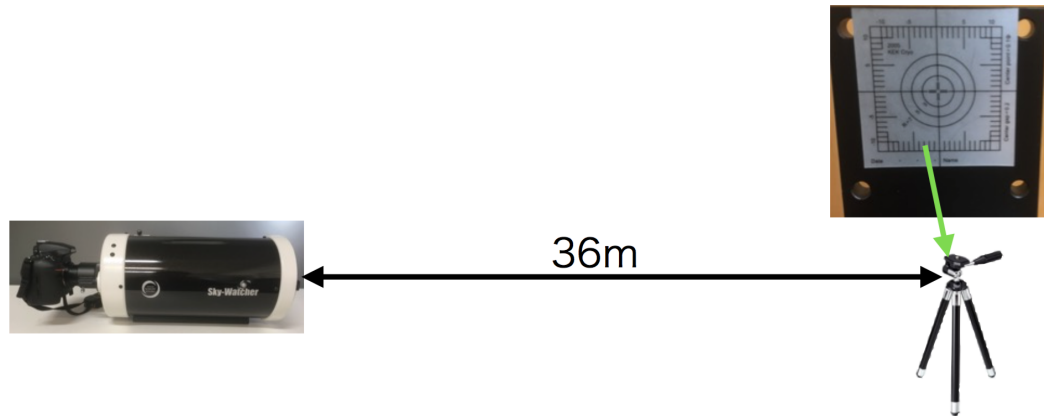


FIGURE 6.2: Setup of demonstration test. We place the camera at 36m far from the ETM. This distance correspond to KAGRA configuration.

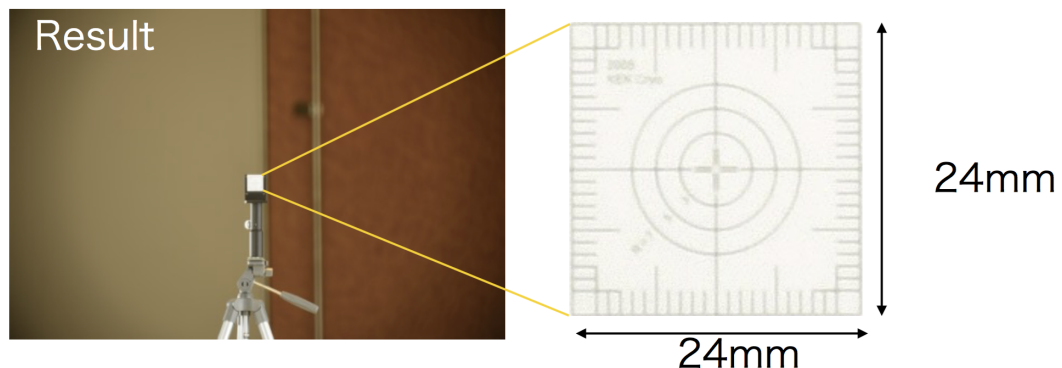


FIGURE 6.3: Raw data of Image analysis (left picture). We are trimming the target region. The size of target is 24×24 mm.

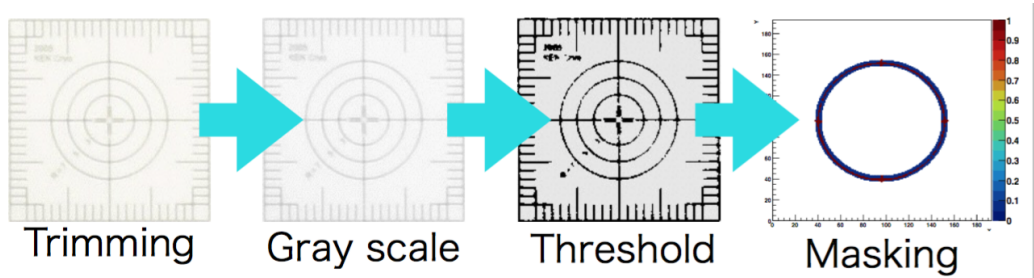


FIGURE 6.4: Strategy of analysis. First we trim the data around the target. Second we convert to Gray scale. Third we set the threshold. Fourth, we pick up the data point using mask.

TABLE 6.1: Fitting result of camera demonstration test.

Parameter	Measured	Expected
R	6.9 ± 0.1 mm	7.0 mm
x_0	11.9 ± 0.1 mm	12.0 mm
y_0	11.9 ± 0.1 mm	12.0 mm

the resolution per one pixel as $24 \text{ mm}/197 \text{ pix.} = 0.12 [\text{mm/pix.}]$. The taken picture is shown in Fig. 6.3.

We are trimming the target region. The trimmed data is converted to gray scale. We set the threshold point at 228. Fig. ?? shows the datas over the threshold. We masked the data points. The process of analysis is shown in Fig. 6.4.

Finally, we have done a fitting and estimate the center point of the circle as shown in Fig. 6.5 and Table. 6.1. Then, we assumed the following equation:

$$y = \sqrt{R^2 - (x - x_0)^2} + y_0. \quad (6.3)$$

The measured and expected parameters are consistent within 1 sigma error. Therefore, it imply that we can estimate the center point with 0.1 mm resolution. In the KAGRA, we use smaller telescope of 127 mm diameter. We estimate the resolution when we use 127 mm telescope. The estimated resolution is $24 \text{ mm}/193 \text{ pix.} \times 150 \text{ mm}/127 \text{ mm} = 0.15 [\text{mm/pix.}]$. It meet our requirement.

6.4 Summary

This chapter has considered the beam position monitor for KAGRA Pcal. The KAGRA photon calibrator is placed at 36 m far from the ETM. This number is larger than that of LIGO and VIRGO. Therefor, the beam position control technique is expected to play a essential role for reducing the systematic error. This system can be applied to LIGO or Virgo as well as KAGRA.

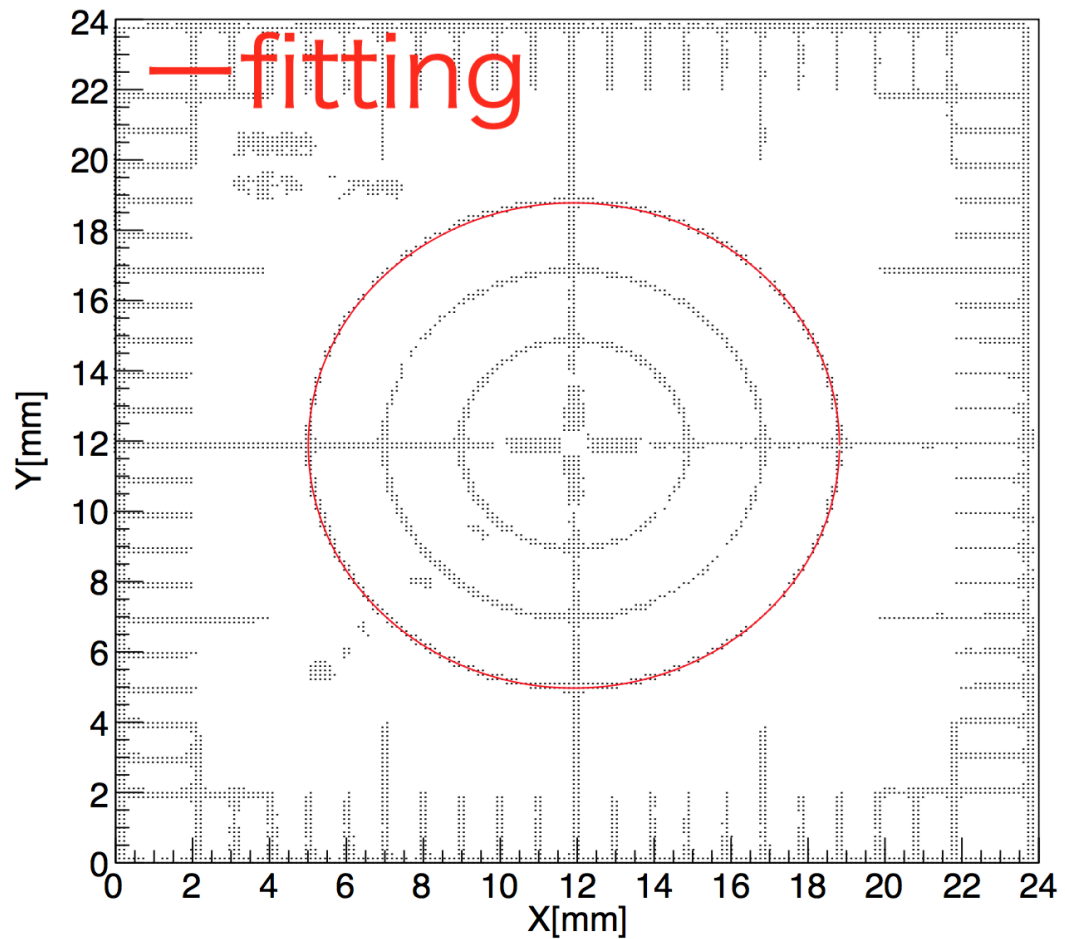


FIGURE 6.5: Fitting result of image analysis. Black dots are data points larger than threshold. We masked data around outer circle. Red circle is best fitting.

Chapter 7

Future upgrades

7.1 Two AOM

The next step would be to design the two AOM system. The system of two AOM can be controlled for upper and lower beam by using two OFS system as shown in Fig. 7.1. Our study has several limitation about modeling studies of the elastic deformation. However, in order to measure high frequency, we need to understand elastic deformation. Current technology is not enough since difference of the upper beam and lower beam are ignore. The strength of this study are well studied to handle various sources of uncertainties. For example, understanding the extent to which Pcal affects the mirror motion will help us set realistic model for analysis. Therefore, it is necessary to develop the technologies for improving systematic error understanding dramatically.

7.2 KAGRA Gold Standard

Photo-detectors used in the transmitter and receiver modules to measure absolute laser power should be calibrated by laser power standard system. The Gold Standard of LIGO (GSL) is calibrated in NIST in US every year. A new test bench to calibrate LIGO PCal photo-detectors were developed in NIST since LIGO PCal uses unpopular wavelength laser of 1047nm to avoid to couple with main laser beam of interferometer with 1064nm in wavelength with keeping sufficient transmittance and reflectivity of optics. Finally, uncertainty of absolute laser power is mainly coming from uncertainty of the standard in NIST.

In fact, absolute laser power is one of the worst precision items in the field of standard. Fig. 7.2 shows performance comparison of laser power standard system in national standard institutions in the world, reported in 2009 [35]. There is large inconsistency of about 4% among the institutions. Rare cross-check of laser power standard among institutions carries out. In future work, we are planning to introduce new test bench of laser power standard with 1047nm in wavelength in AIST(National Institute of Advanced Industrial Science and Technology) in Japan. We have already started discussion of such test bench development with a scientist in AIST. We newly make the Gold standard of KAGRA (GSK) using the integrating sphere with photo detector. By comparison with laser power standards both in NIST and AIST, and also with GSL and GSK themselves between aLIGO and KAGRA, we evaluate systematic errors of PCals, and achieve to improve its accuracy. To calibrate the WSK, we plan to make a optical bench in Toyama university as shown in Fig. 7.3. We will bring and compare the calibrated WSK and GSL in LHO.

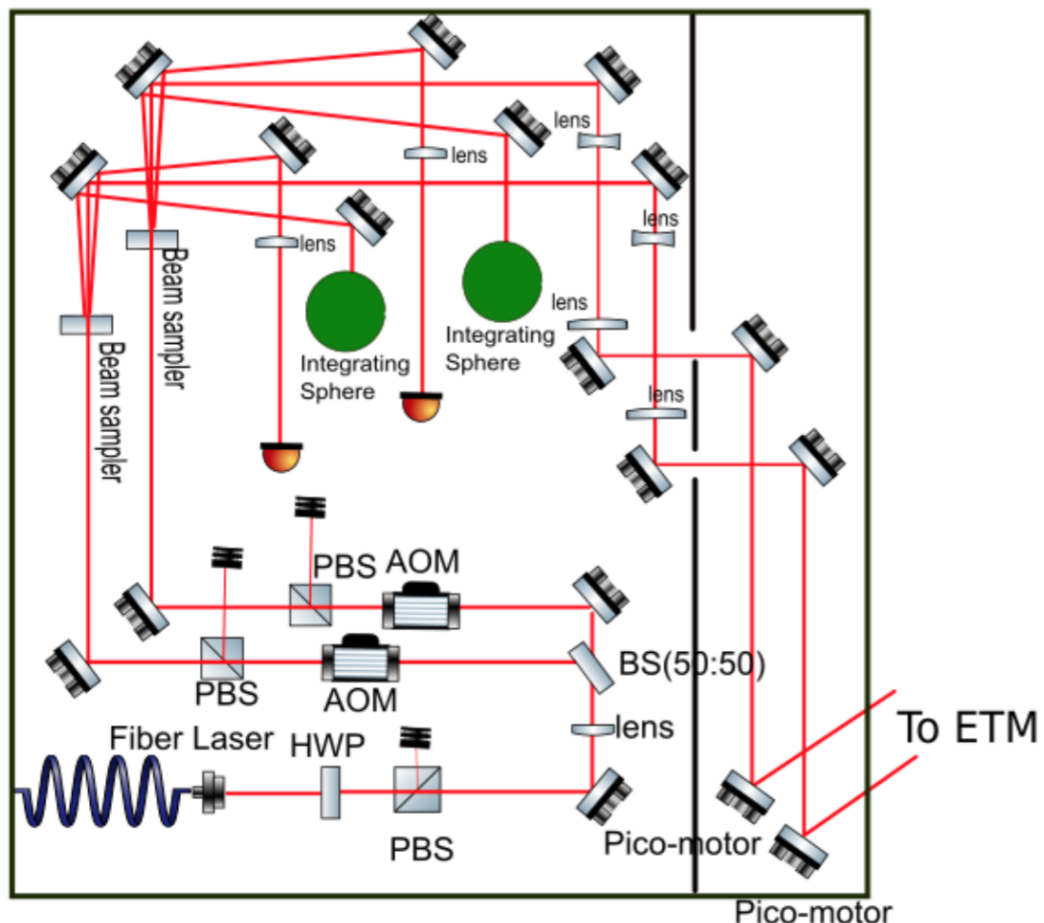


FIGURE 7.1: Transmitter module with two AOM system.

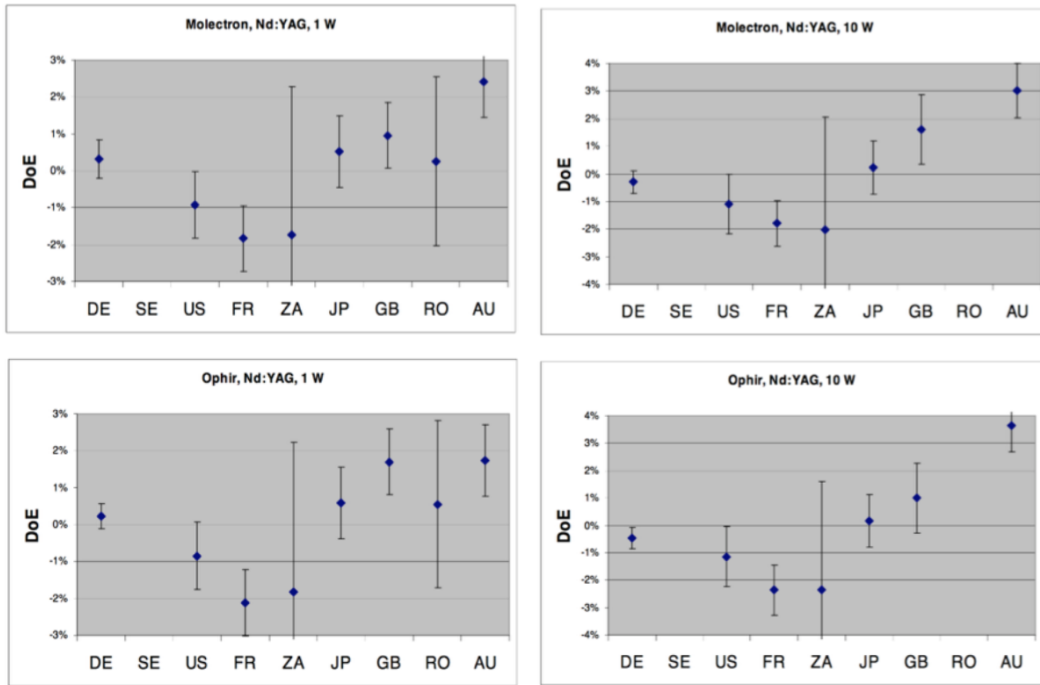


FIGURE 7.2: Performance comparison of laser power standard system at 1064nm wavelength and 1W power in the national standard institutions in the world [35].

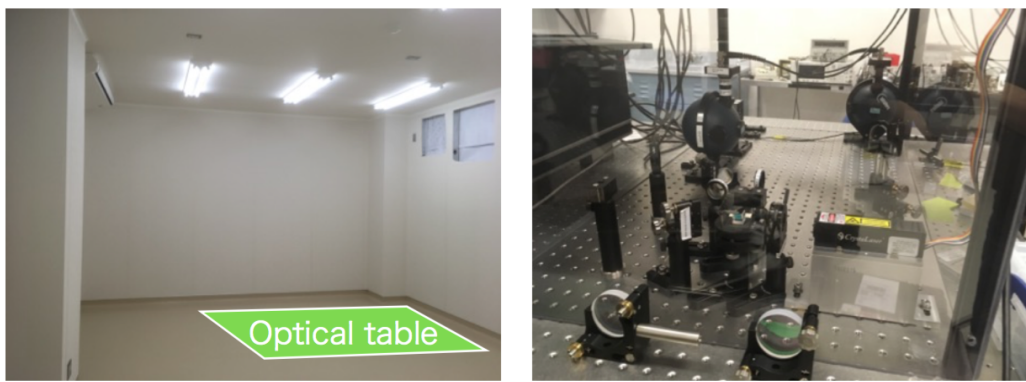


FIGURE 7.3: .

Chapter 8

Summary

Accurate calibration of the output of the Gravitational Wave (GW) signal is essential to determine the physics parameters of the astronomical sources. This document has considered the design of the KAGRA photon calibrator. This study is an important contribution for world wide observation because the calibration accuracy of each interferometer is based on the combine analysis. The challenge now is to realize these possibility.

Appendix A

Propagation of calibration errors into the estimated source parameters

In order to understand the propagation of systematic errors from calibration parameters to the estimated source parameters, a simple simulation is made as follows.

A.1 DARM feedback loop modeling

As discussed in Chapter 2, the response function of interferometer system $R(f)$ can be written as

$$R(f) = \frac{1 + G(f)}{C(f)} \quad (\text{A.1})$$

where $G(f) = C(f)D(f)A(f)$ is the DARM open loop gain, $C(f)$ is the sensing function, $D(f)$ is the digital filters and $A(f)$ is the actuator function. As a typical configuration, we used $G(f)$ and $A(f)$ based on the LIGO O1/O2 configuration [4, 14]. Fig. A.1 shows the transfer functions of open loop gain and actuators. Here we assume the three-stage pendulum and second and third stages contribute the control in the frequency range we are interested in. For the sensing function, in the case without Signal Recycling Cavity (SRC) detuning, $C(f)$ can be approximated by a single pole,

$$C(f) = \frac{G_c}{1 + if/f_c}, \quad (\text{A.2})$$

where G_c is the optical gain, f_c is the coupled cavity pole frequency.

In this simulation, we assume three parameters, G_c , f_c and A_T to be calibrated and tracked, where A_T is the scale factor of the actuator function. Figs. A.2, A.3 and A.4 show the deformations of $R(f)$ due to the calibration bias on these three parameters. These results agree with Ref [14]. Since the assumed transfer functions are not exactly the same as Ref [14] there are minor differences.

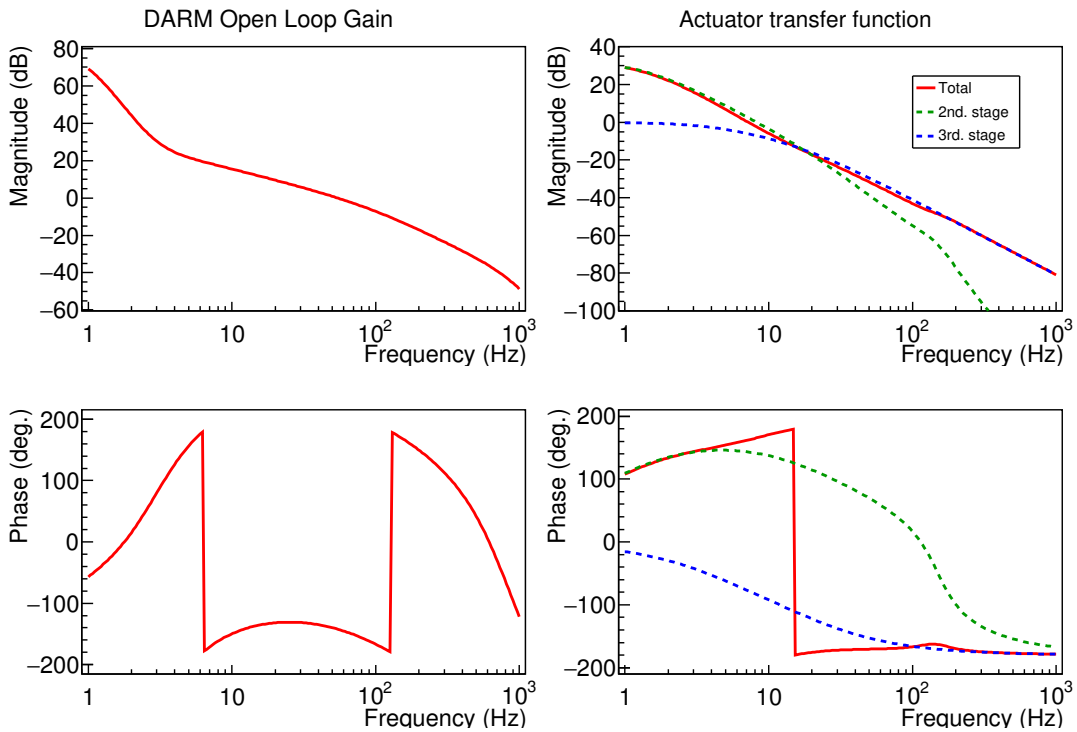


FIGURE A.1: Transfer functions of DARM open loop gain and actuators assumed in this simulation.

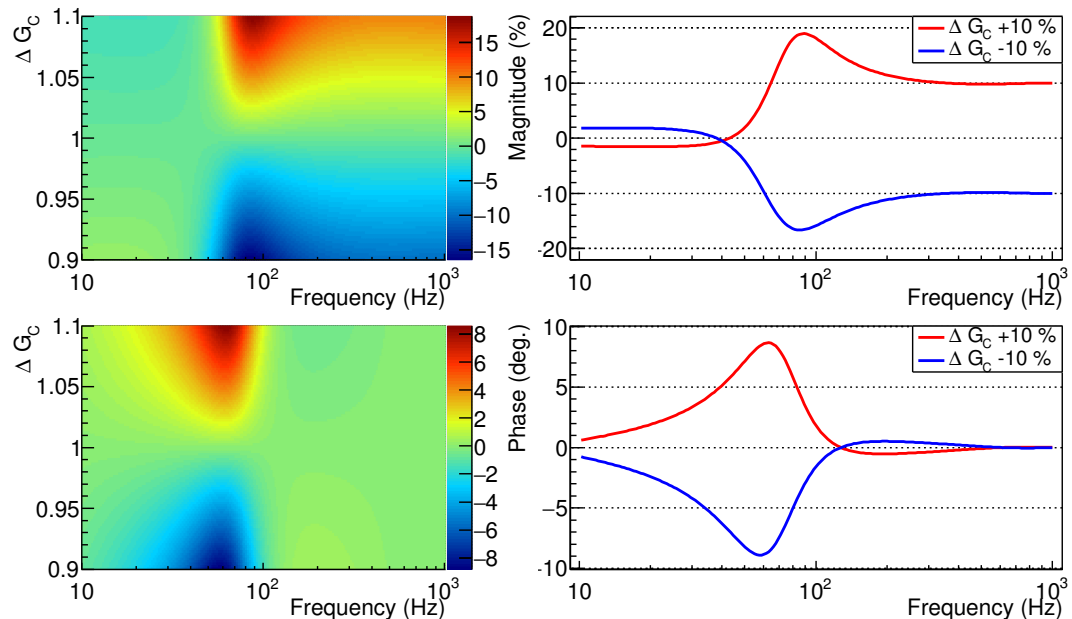


FIGURE A.2: Deformation of $R(f)$ due to the relative calibration bias on G_C .

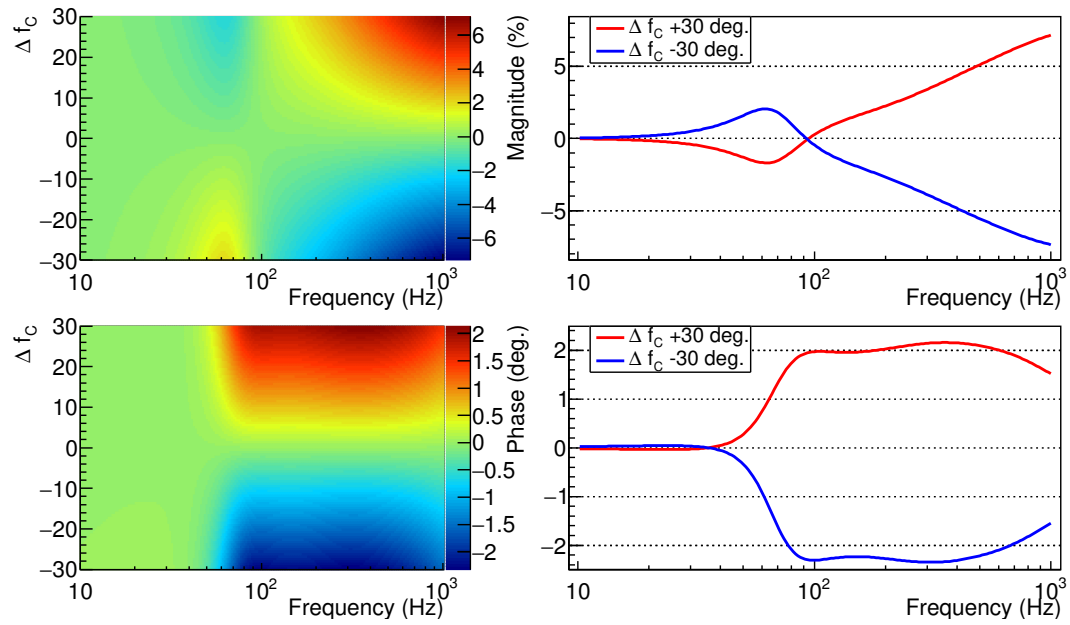


FIGURE A.3: Deformation of $R(f)$ due to the relative calibration bias on f_C .

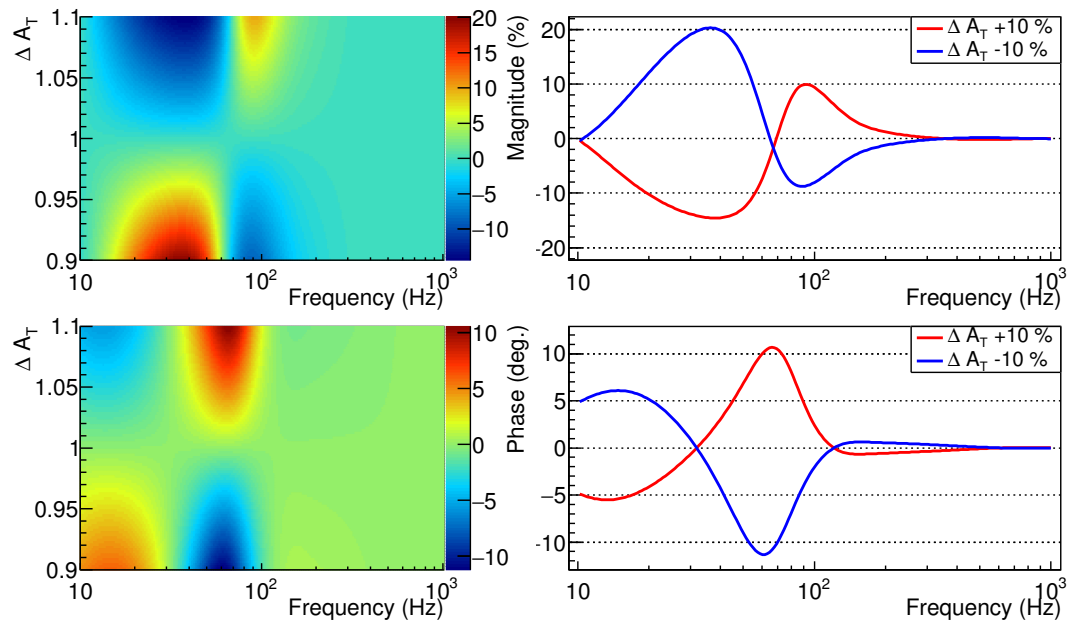


FIGURE A.4: Deformation of $R(f)$ due to the calibration bias on A_T .

A.2 Waveform modeling

As a simple example, we assume the GW signal in the frequency domain from the compact binary coalescence by using the second order post-Newtonian (2-pN) formalism and ignoring any effects due to the spins with five free parameters, a total system mass, $M = m_1 + m_2$, a symmetric mass ratio $\eta = m_1 m_2 / M^2$, the source distance, D , a coalescence time t_c , and a coalescence phase ϕ ,

$$h(f) = \frac{1}{2\pi^{2/3} c^{3/2}} \frac{(GM)^{5/6}}{D} \left(\frac{5\eta}{6} \right)^{1/2} f^{-7/6} e^{i(2\pi f t_c + \phi + \Psi(f))}, \quad (\text{A.3})$$

where

$$\Psi(f) = \sum_{i=1}^4 a_i \xi_i(f), \quad (\text{A.4})$$

$$a_1 = \frac{3}{128\eta} q^{-5/3}, \quad (\text{A.5})$$

$$a_2 = \frac{1}{384\eta} \left(\frac{3715}{84} + 55\eta \right) q^{-1}, \quad (\text{A.6})$$

$$a_3 = -\frac{1}{128\eta} 48\pi q^{-2/3}, \quad (\text{A.7})$$

$$a_4 = \frac{3}{128\eta} \left(\frac{15293365}{508032} + \frac{27145}{504}\eta + \frac{3085}{72}\eta^2 \right) q^{-1/3}, \quad (\text{A.8})$$

$\xi_1(f) = f^{-5/3}$, $\xi_2(f) = f^{-1}$, $\xi_3(f) = f^{-2/3}$, $\xi_4(f) = f^{-1/3}$, and $q = \pi G M c^{-3}$ [36].

The parameters estimation is done with the maximum likelihood method,

$$\ln L = -\frac{1}{2} \int_{f_{min}}^{f_{max}} df \frac{|d(f) - h(f)|^2}{S(f)}, \quad (\text{A.9})$$

where f_{min} and f_{max} are the filtered frequency range, $d(f)$ and $h(f)$ are observed and estimated wave forms, and $S(f)$ is the power spectrum density of the detector noise.

In this analysis we assume the source parameters similar to GW150914 and fittin between 30 and 300 Hz. Fig. A.5 shows the comparisons of relative deformed and fitted wave forms with respect to the true one. Finally, we estimated the bias on the five source parameters. Left part of Fig. A.6 shows the systematic bias on the five source parameters, while right part of Fig. A.6 shows the extreme case where the source distance is 200 Mpc away and the signal-to-noise ratio is high enough.

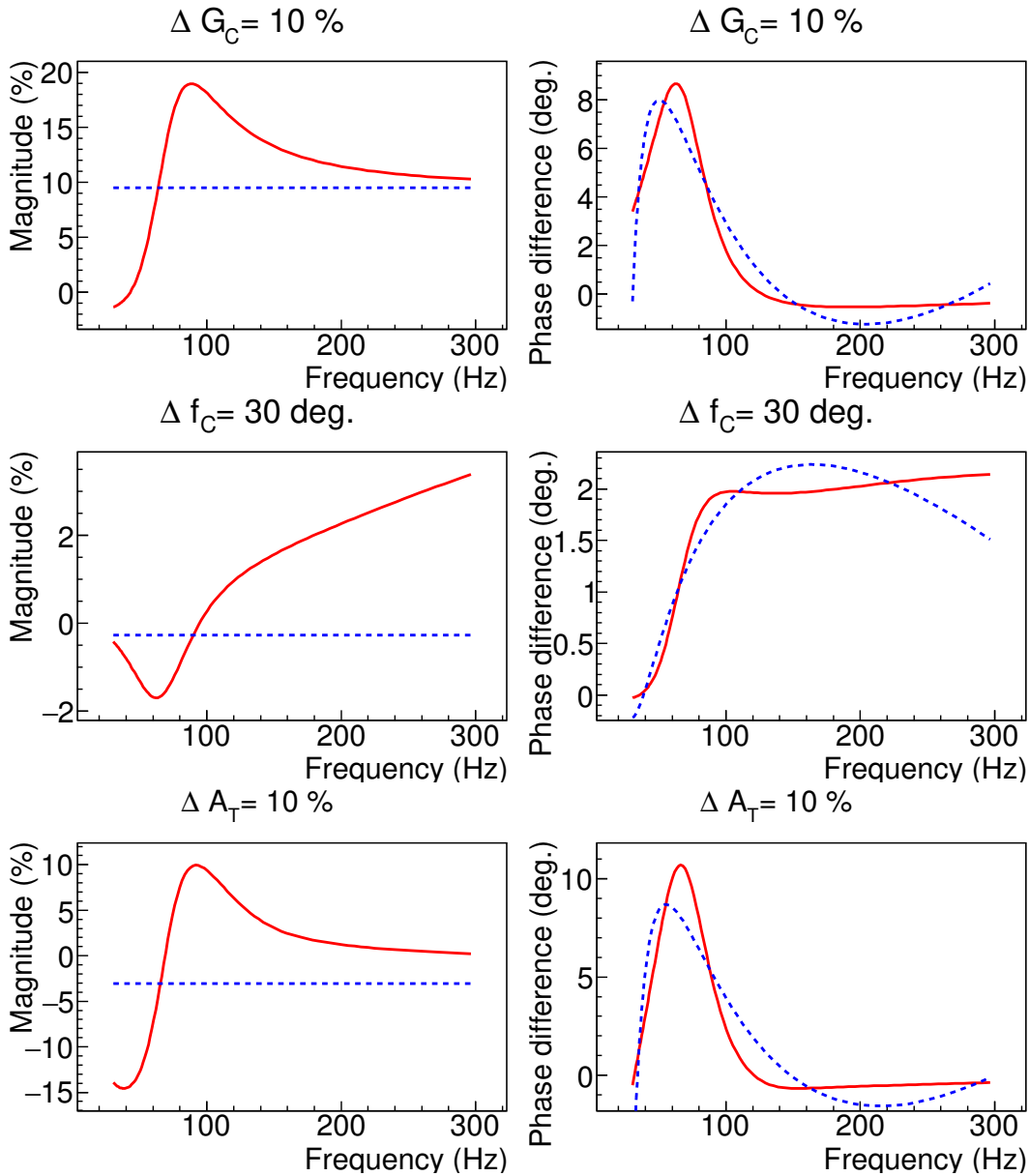


FIGURE A.5: Comparisons of relative deformed (red solid lines) and fitted (blue dashed lines) wave forms with respect to the true one, in the three cases where G_C , f_C and A_T are biased by $\pm 10\%$, ± 30 deg., and $\pm 10\%$, respectively.

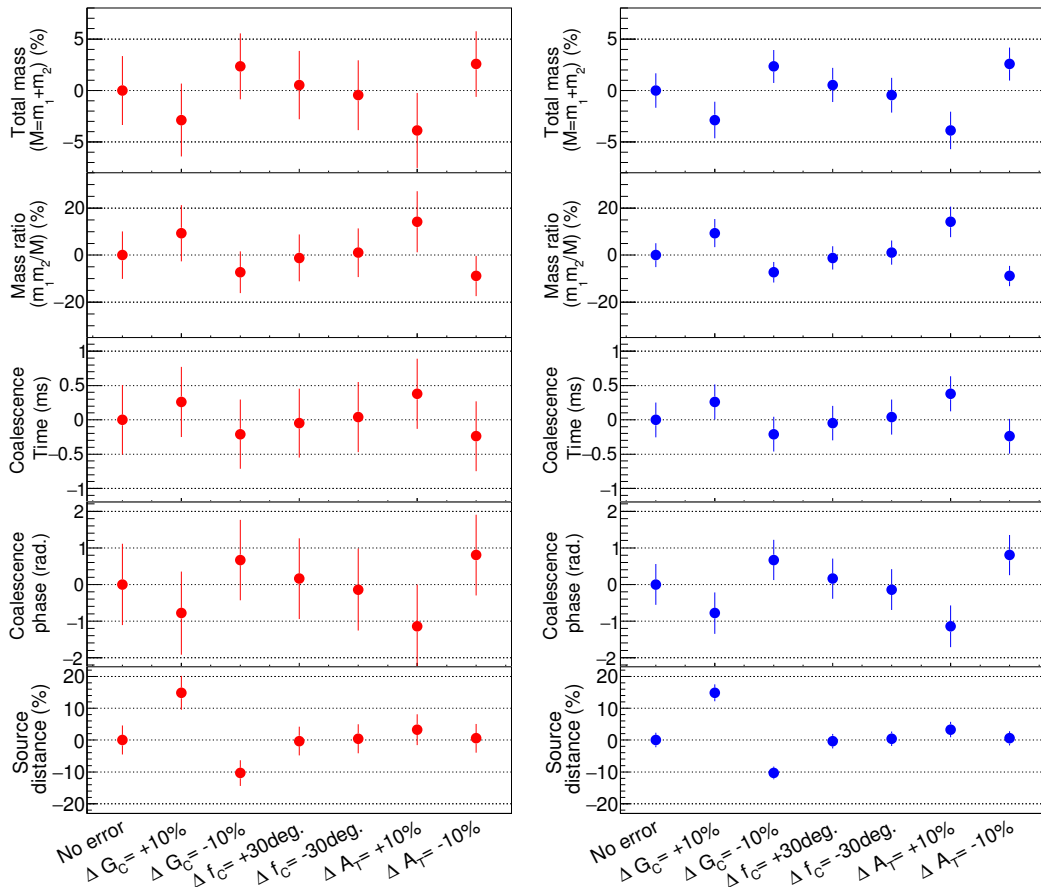


FIGURE A.6: The systematic bias on the five source parameters as a function of variations of calibration parameters assuming the signal similar to GW150914 (left), and the extreme case where the GW150914 source is 200 Mpc away (right).

Bibliography

- ¹B. P. Abbott, et al., “Observation of Gravitational Waves from a Binary Black Hole Merger”, [Phys. Rev. Lett. **116**, 061102 \(2016\)](#).
- ²B. P. Abbott, et al., “GW151226: Observation of Gravitational Waves from a 22-Solar-Mass Binary Black Hole Coalescence”, [Phys. Rev. Lett. **116**, 241103 \(2016\)](#).
- ³S. Klimenko, G. Vedovato, M. Drago, G. Mazzolo, G. Mitselmakher, C. Pankow, G. Prodi, V. Re, F. Salemi, and I. Yakushin, “Localization of gravitational wave sources with networks of advanced detectors”, [Phys. Rev. **D83**, 102001 \(2011\)](#).
- ⁴B. P. Abbott, et al., “Calibration of the Advanced LIGO detectors for the discovery of the binary black-hole merger GW150914”, [arXiv **1602**, 03845 \(2016\)](#).
- ⁵S. Karki, et al., “The Advanced LIGO Photon Calibrators”, [Rev. Sci. Instrum. **87**, 114503 \(2016\)](#).
- ⁶L. Rolland, F. Marion, and B. Mours, “Conceptual design of advanced virgo photon calibration”, [Virgo TDS **0013A**, 15 \(2015\)](#).
- ⁷T. Accadia, et al., “Reconstruction of the gravitational wave signal $h(t)$ during the Virgo science runs and independent validation with a photon calibrator”, [Class. Quant. Grav. **31**, 165013 \(2014\)](#).
- ⁸D. A. Clubley, G. P. Newton, K. D. Skeldon, and J. Hough, “Calibration of the Glasgow 10-m prototype laser interferometric gravitational wave detector using photon pressure”, [Phys. Lett. **A283**, 85–88 \(2001\)](#).
- ⁹K. Mossavi, M. Hewitson, S. Hild, F. Seifert, U. Weiland, J. R. Smith, H. Luck, H. Grote, B. Willke, and K. Danzmann, “A photon pressure calibrator for the GEO 600 gravitational wave detector”, [Phys. Lett. **A353**, 1–3 \(2006\)](#).
- ¹⁰E. Goetz, et al., “Precise calibration of LIGO test mass actuators using photon radiation pressure”, [Class. Quant. Grav. **26**, 245011 \(2009\)](#).
- ¹¹B. Mours, and L. Rolland, “Determining the sign of h-rec with the photon calibrator”, [Virgo TDS **018A**, 07 \(2007\)](#).
- ¹²B. P. Abbott, et al., “Prospects for observing and localizing gravitational-wave transients with advanced ligo and advanced virgo”, [Living Reviews in Relativity **19**, 1 \(2016\)](#).
- ¹³M. Ando, “Observation Scenario Paper”, [JGW **G1706116** \(2017\)](#).
- ¹⁴D. Tuyenbayev, et al., “Improving LIGO calibration accuracy by tracking and compensating for slow temporal variations”, [Class. Quant. Grav. **34**, 015002 \(2017\)](#).
- ¹⁵E Hall, “Calibrating optical springs”, [LIGO-DCC, G1601599 \(2016\)](#).
- ¹⁶ Thorlabs,
- ¹⁷ Keopsys,
- ¹⁸ lasermet, “Ls-10-12”,
- ¹⁹C. laser optics,

- ²⁰ Polarizer, "Tfpcl2-1047",
- ²¹ JamMt,
- ²² Sigma-koki,
- ²³ Newport,
- ²⁴I. laser optics,
- ²⁵ Excelitas,
- ²⁶ Labsphere, "Spectralon",
- ²⁷ Cosmotech,
- ²⁸ANSYS®Academic Research, Release **17.1** (2016).
- ²⁹ D810,
- ³⁰ Skywatcher, "Maksutov-cassegrain",
- ³¹E. MEDM,
- ³²S. Hild, et al., "Photon pressure induced test mass deformation in gravitational-wave detectors", [Class. Quant. Grav. **24**, 5681–5688 \(2007\)](#).
- ³³H. P. Daveloza, M Afrin Badhan, M Diaz, K Kawabe, P. N. Konverski, M Landry, and R. L. Savage, "Controlling calibration errors in gravitational-wave detectors by precise location of calibration forces", [Journal of Physics: Conference Series **363**, 012007 \(2012\)](#).
- ³⁴COMSOL®Multiphysics, Release **5.2a** (2016).
- ³⁵S. Kuck, "Responsivity of detectors for radiant power of lasers, final report, edited by stefan kuck", EUROMET Comparison Project **156**, EUROMET.PR-S2 (2009).
- ³⁶T. Tanaka, and H. Tagoshi, "The Use of new coordinates for the template space in hierarchical search for gravitational waves from inspiraling binaries", [Phys. Rev. **D62**, 082001 \(2000\)](#).